Additive Manufacturing 86 (2024) 104155

Contents lists available at ScienceDirect

Additive Manufacturing

journal homepage: www.elsevier.com/locate/addma

Continuous fiber path optimization in additive manufacturing: A gradient-based B-spline finite element approach

Shuaiyin He [a], Peng-Cheng Ma [c], Molong Duan [a,b,*]

[a] Department of Mechanical and Aerospace Engineering, The Hong Kong University of Science and Technology, Hong Kong Special Administrative Region of China
[b] HKUST Shenzhen-Hong Kong Collaborative Innovation Research Institute, Futian, Shenzhen, China
[c] Laboratory of Environmental Science and Technology, The Xinjiang Technical Institute of Physics and Chemistry, Key Laboratory of Functional Materials and Devices for Special Environments, Chinese Academy of Sciences, Urumqi, China

ARTICLE INFO

Keywords:
Continuous fiber path optimization
Composite additive manufacturing
Finite element model
Trajectory generation

ABSTRACT

Additive manufacturing of continuous fiber enables the control of local material distribution and mechanical characteristics. This localized control is realized through fiber path generation and optimization, which is one of the core problems in the additive manufacturing of continuous fiber. Current fiber path generation and optimization methods mostly try to infill topology-optimized parts or align the fiber with the maximum stress directions, which may lead to sub-optimality or time-consuming computations. This paper provides a different approach to optimize the fiber path directly by parameterizing it with B-splines and manipulating its control points. A finite element model with B-spline fiber parameterization is established, with an analytical fiber-in-element probability. This framework streamlines the computation of local and global stiffness and mass matrices, enabling effective and efficient prediction of loading responses, stiffness, and natural frequencies. The probability framework also allows efficient calculation of the gradients of the stiffness and mass matrices, leading to a gradient-based fiber path optimization. The effectiveness and accuracy of both the finite element and optimization methods are verified with simulation and experiment case studies. Results demonstrate enhancements in stiffness and strength with less fiber usage compared to a commonly adopted principal stress direction method.

1. Introduction

Continuous-fiber-reinforced parts are widely adopted in aircraft, automobiles, energy, and sports applications due to their benefits of light weight, high stiffness, and high strength [1,2]. The fiber-reinforced parts are typically categorized into standard components (e.g., laminate sheets and tubes) or geometrically complex parts. For standard components, conventional manufacturing methods such as pultrusion, filament winding, and co-weaving provide efficient and cost-effective mass production [3]. For geometrically complex parts, manual layup, resin transfer molding, spray deposition, and vacuum bagging are typically used [3]. However, these conventional methods of manufacturing geometrically complex parts typically require a high-cost mold, which limits its usage in small batch, customized production. Moreover, these methods yield uniform fiber directions, which do not fully exploit the anisotropic properties of the fiber [4]. Recently, there is a trend to tailor the manufactured parts' regional and directional mechanical properties [5]. This trend of optimizing the part's reliability, strength, weight, and cost requires non-uniform fiber distributions and orientations to achieve more complex and coupled goals (e.g., enhanced stiffness/strength [6], lower fiber usage [7], tailored frequency response [8], etc.). To satisfy these goals, local fiber path manipulation is essential, and it is typically achieved by the robotic-based fiber tow steering [9,10] or material extrusion (MEX) with continuous fiber. The fiber tow steering is desirable for high fiber volume ratio, large scale, and low curvature structures (e.g., aircraft fuselage) but may suffer from issues of discontinuity, delamination, and wrinkle [9]. On the other hand, the MEX with continuous fiber has higher fiber path design degrees of freedom and has enhanced performances with fiber paths with higher curvature [11–15]. Continuous fiber has also been proven to significantly enhance the mechanical properties of fiber-reinforced parts compared to MEX with short fiber [16,17] due to its continuity and controllable fiber directions

---

[*] Corresponding author at: Department of Mechanical and Aerospace Engineering, The Hong Kong University of Science and Technology, Hong Kong Special Administrative Region of China.

E-mail address: duan@ust.hk (M. Duan).

https://doi.org/10.1016/j.addma.2024.104155
Received 2 October 2023; Received in revised form 10 April 2024; Accepted 21 April 2024
Available online 12 May 2024

[18–21]. In this research, the MEX with continuous fiber is the core focus and application use cases.

Despite the high degree of freedom of continuous fiber path in the MEX process, generation of the fiber and matrix printing path is still challenging. Unlike conventional MEX processes where the printing paths are generated from straightforward shape and infill ratio information [22], the generation of fiber paths demands a holistic optimization of the mechanical behavior analysis of non-uniform fiber distribution and orientation. This optimization in fiber path is not supported in most commercial MEX print path software [22]. To fill this gap, many researchers focus on fiber path generation and optimization methods considering the part's mechanical properties. Fernandes et al. [23] developed offset and equally spaced methods to infill the fiber paths in a topology-optimized homogeneous part without fiber reinforcements. Another mainstream approach generates the fiber paths by maximizing their alignment with the stress field of a homogeneous part without fiber reinforcements [24]. The load-dependent path planning method [25] introduces an optimization problem to align the fiber and local load directions. Liu et al. [26] proposed a wave projection function to design the fiber paths infill in the stress field. Chen et al. [27] converted the stress vector field into a scalar field to compute distributed fiber paths directly in the design space. However, these methods are based on the stress field of a homogeneous part without fiber reinforcement; the fiber's contribution to the stress field is thus not considered. Notably, the stress field of a fiber-reinforced part and a homogeneous part can be significantly different [28]. Therefore, to further achieve various fiber path design objectives, the stress field of the fiber-reinforced parts needs to be considered.

The challenge of exploiting the fiber-reinforced parts arises because they have to be calculated with a set of determined fiber paths, which is simultaneously the optimization variable. Accordingly, iterative optimizations are frequently used to address this issue. Suzuki et al. [29] iteratively calculated the stress tensor and stiffness decay vector to construct the finer orientations. Kentaro et al. [30] adopted a similar idea while introducing the regional fiber volume ratio to represent the distance between fiber paths. Hou et al. [31] introduced fiber track points to extract the fiber path from every iteration's stress field; the nearest point on the extracted path determines the fiber orientations and distributions inside an element. Papapetrou et al. [32] introduced a finite element model with variables of fiber direction and density in the optimization, and then infilled the topology-optimized parts with different continuous fiber placement strategies (i.e., offset, equally-space, streamline). These methods consider the fiber's contribution to the stress field but still have two major issues. Firstly, the fibers are discretized in a mesh and thus require a significant amount of computations to determine the fiber and mesh element relationship. This computation can be time-consuming and leads to non-smoothness in the optimization, resulting in local optimums. Secondly, this type of methods typically requires multi-stage optimization (e.g., generation of the optimal stress field and fiber path fitting); the multi-stage optimization may yield sub-optimal solutions.

To address these issues, this paper proposes a gradient-based approach that parametrized the fiber path with B-spline, along with a customized finite element model (FEM) with continuous fiber contributions. The main contributions of the paper are:

- This paper establishes a computationally efficient semi-analytical FEM compatible with arbitrary fiber paths by an analytically determined fiber-in-element probability.
- The paper developed a computationally efficient potential function in controlling the fiber-to-fiber and fiber-to-boundary distance in fiber path optimization.
- With the semi-analytical FEM with gradients, a gradient-based B-spline fiber path optimization compatible with multiple objective functions (e.g., compliance, fiber usage, frequency response, etc.) is developed and verified in numerical and experimental case studies.

The paper is structured as follows: The FEM with B-spline parameterization is detailed in Section 2, in which the local mass and stiffness matrix exploiting the analytical fiber-in-element probability and convex hull of the B-spline are derived and discussed. The section also covers the assembly of the global mass and stiffness matrix to acquire the detailed stress, strain, and compliance under certain loading conditions, as well as the natural frequencies and the mode shapes of the fiber-reinforced parts. In Section 3, the semi-analytical gradients of the FEM concerning the B-spline control points are derived. These gradients, with the help of a customized fiber distancing function with a potential field, enable a gradient-based B-spline fiber path optimization. The FEM with B-spline parameterization and the gradient-based B-spline fiber path optimization are verified in simulation and experiments in Section 4, followed by conclusions in Section 5.

2. Finite element model with B-spline fiber parameterization

This paper's proposed approaches aim to establish a finite element model that considers the continuous fiber path parameterized with B-spline. The B-spline fiber path through the elements provides local reinforcement by changing the local element mass and stiffness matrices. This approach encourages fiber path iterations and optimization as it does not require re-meshing of the fiber and matrix regions. Compared to other high-order, high-fidelity models generated by the FEM commercial software (e.g., Ansys, Abaqus, etc.), this approach enhances computational efficiency and is more compatible with fiber path optimizations. The workflow of this approach is shown in Fig. 1. The green block in the chart is the main content of this section, which includes the establishment of the stiffness and mass matrices in the typical FEM and the fiber reinforcement analysis by B-spline parameterization. As the key to this approach, the pink block introduces the identification of the fiber-reinforced candidate by the convex hull of the B-spline, and the analytical probability function to locate the fiber in each candidate. The increments to the stiffness and mass matrices are obtained based on the distribution of each fiber in the elements. Then, the global matrices are assembled with the initial matrices and the increments.

2.1. Finite element modeling framework of parts with continuous fiber

Consider a 2-dimensional (2D) region $\mathscr{V}$ that requires a fiber reinforcement shown in Fig. 2(a). The boundary of the regions is defined as $\partial\mathscr{V}$. Without loss of generality, three-node triangular elements are exploited to discrete the region Ω (the method also applies to other types of meshes) shown in Fig. 2(b). It is assumed that the mesh's characteristic size is significantly smaller than the fiber's achievable radius of curvature. Note that this work focuses on compliance minimization and fiber usage optimization; the fiber-reinforced parts are assumed to work in their elastic regions. Therefore, slippage in the fiber matrix contact regions is omitted during the modeling process. These assumptions are widely adopted in fiber-reinforced parts stiffness calculations, such as in the volume average stiffness (VAS) model [33].

Define the displacement field $u(x,y),\ v(x,y)$. Inside one triangular element, the displacement field is given by

$$\begin{cases} u(x,y) = S_1(x,y)u_1 + S_2(x,y)u_2 + S_3(x,y)u_3 \\ v(x,y) = S_1(x,y)v_1 + S_2(x,y)v_2 + S_3(x,y)v_3 \end{cases}, \tag{1}$$

where u_i and v_i are Node P_i's displacement in the x and y axes, for i=1,2,3 respectively. Define (x_i, y_i) to be the Node P_i's coordinates, and the shape function $S_i(x,y)$ is given by:

$$S_i(x,y) = \frac{1}{2A}(a_i + b_i x + c_i y),\ i = 1,2,3, \tag{2}$$

where,

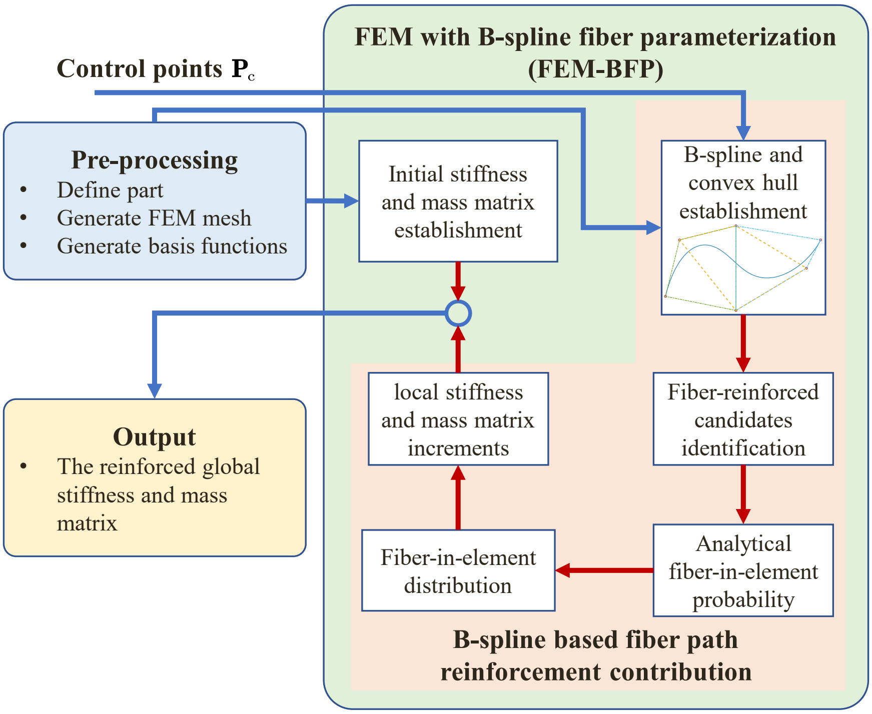

Fig. 1. Finite element model with B-spline fiber parameterization flow chart.

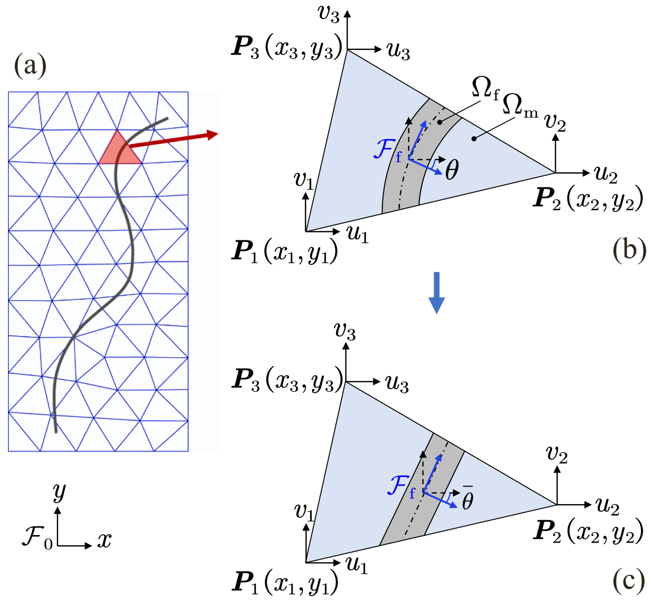

Fig. 2. Three-node triangular element with fiber.

$$A=\frac{1}{2}(a_1+a_2+a_3)=\frac{1}{2}(b_1c_2-b_2c_1), \tag{3}$$

$$\begin{cases} a_1=x_2y_3-x_3y_2\\ b_1=y_2-y_3\\ c_1=-x_2+x_3 \end{cases}. \tag{4}$$

The coefficients a_i, b_i, c_i for $i=2,3$ follow the same formulas as in Eq. (4) by circular alternating the subscript (i.e., 1→2, 2→3, 3→1). The displacement field relationship in the eth element is written in the matrix form as:

$$\mathbf{u}^{(e)}(x,y)=\begin{bmatrix}u\\v\end{bmatrix}=\underbrace{\begin{bmatrix}S_1&0&S_2&0&S_3&0\\0&S_1&0&S_2&0&S_3\end{bmatrix}}_{\mathbf{S}(x,y)}\mathbf{q}^{(e)}, \tag{5}$$

where $\mathbf{S}(x,y)$ is shape function matrix and $\mathbf{q}^{(e)}$ is the nodal degrees of freedom given by:

$$\mathbf{q}^{(e)}=\begin{bmatrix}u_1 & v_1 & u_2 & v_2 & u_3 & v_3\end{bmatrix}^{\top}. \tag{6}$$

As the linear displacement relationship indicated in Eq. (1), note that the strain field is assumed constant in the triangular element, regardless of fiber or the matrix region. The strain is written as:

$$\boldsymbol{\varepsilon}^{(e)}=\begin{bmatrix}\varepsilon_{xx}{}^{(e)} & \varepsilon_{yy}{}^{(e)} & \gamma_{xy}{}^{(e)}\end{bmatrix}^{\top}=[\partial]\mathbf{u}^{(e)}, \tag{7}$$

where $[\partial]$ is operator matrix defined as:

$$[\partial]=\begin{bmatrix}\dfrac{\partial}{\partial x} & 0\\ 0 & \dfrac{\partial}{\partial y}\\ \dfrac{\partial}{\partial y} & \dfrac{\partial}{\partial x}\end{bmatrix}. \tag{8}$$

Substitute Eq. (5) into Eq. (7), the element strain is given by:

$$\boldsymbol{\varepsilon}^{(e)}=[\partial]\mathbf{S}(x,y)\mathbf{q}^{(e)}=\mathbf{B}(x,y)\mathbf{q}^{(e)}, \tag{9}$$

where $\mathbf{B}(x,y)$ is the conventional geometry matrix for triangular mesh. The formula in Eqs. (1) to (9) satisfies conventional FEM formulations as in [34].

Unlike the strain relationship that is constant within the matrix and fiber region, the stress field $\boldsymbol{\sigma}(x,y)$ is not consistent in the fiber and matrix regions due to their significantly different constitutive relationships, i.e.,

$$\boldsymbol{\sigma}(x,y)=\begin{bmatrix}\sigma_{xx}(x,y)\\ \sigma_{yy}(x,y)\\ \tau_{xy}(x,y)\end{bmatrix}=\begin{cases}\mathbf{D}_m\boldsymbol{\varepsilon} & \text{when } (x,y)\in\Omega_m\\ \mathbf{D}_f\boldsymbol{\varepsilon} & \text{when } (x,y)\in\Omega_f\end{cases}, \tag{10}$$

where $\mathbf{D}_\mathrm{m}$ is the elastic coefficient matrix in the isotropic matrix region Ω_m and $\mathbf{D}_\mathrm{f}$ is the elastic coefficient matrix in the fiber-reinforced region Ω_f, respectively. Define the isotropic matrix material with Young's modulus E_m and Poisson ratio μ, the elastic coefficient matrix $\mathbf{D}_\mathrm{m}$ is given by:

$$\mathbf{D}_\mathrm{m} = \frac{E_\mathrm{m}}{1-\mu^2}\begin{bmatrix} 1 & \mu & 0 \\ \mu & 1 & 0 \\ 0 & 0 & \dfrac{1-\mu}{2} \end{bmatrix}. \tag{11}$$

Similarly, in the fiber-reinforced region Ω_f, the longitudinal and transverse Young's moduli are defined as E_1 and E_2, respectively. The in-plane Poisson ratios are defined as μ_{12} ($\mu_{21} = \mu_{12}E_2/E_1$); the shear modulus is defined as G_{12}, the elastic coefficient matrix $\mathbf{D}_\mathrm{f}$ is given by:

$$\mathbf{D}_\mathrm{f} = \mathbf{T}(\theta)^\top \underbrace{\begin{bmatrix} \dfrac{E_1^2}{E_1 - E_2\mu_{12}^2} & \dfrac{E_1E_2\mu_{12}}{E_1 - E_2\mu_{12}^2} & 0 \\ \dfrac{E_1E_2\mu_{12}}{E_1 - E_2\mu_{12}^2} & \dfrac{E_1E_2}{E_1 - E_2\mu_{12}^2} & 0 \\ 0 & 0 & G_{12} \end{bmatrix}}_{\triangleq \mathbf{D}_{\mathrm{f}0}} \mathbf{T}(\theta), \tag{12}$$

where θ is the angle between the fiber primary coordinate frame $\mathscr{F}_\mathrm{f}$ to the ground frame $\mathscr{F}_0$ shown in Fig. 2(c), and $\mathbf{T}(\theta)$ is the transformation matrix given by:

$$\mathbf{T}(\theta) = \begin{bmatrix} \cos^2\theta & \sin^2\theta & 2\sin\theta\cos\theta \\ \sin^2\theta & \cos^2\theta & -2\sin\theta\cos\theta \\ -\sin\theta\cos\theta & \sin\theta\cos\theta & \cos^2\theta - \sin^2\theta \end{bmatrix}. \tag{13}$$

The FEM is established via the principle of virtual work. Define the vector collection of all nodal degrees of freedom to be $\mathbf{q}$, the eth element's nodal displacement $\mathbf{q}^{(e)}$ formulates a subset of $\mathbf{q}$ defined with a selector matrix $\mathbf{T}_e$, i.e.,

$$\mathbf{q}^{(e)} = \mathbf{T}_e\mathbf{q}, \tag{14}$$

The total potential energy Π expressed by displacement $\mathbf{u}$, strain $\boldsymbol{\varepsilon}$, and stress $\boldsymbol{\sigma}$ given by:

$$\begin{aligned} \Pi &= U - W_\mathrm{b} - W_\mathrm{p} - W_\mathrm{s} - W_\mathrm{I} \\ &= \frac{1}{2}\int_{\mathscr{V}} \boldsymbol{\varepsilon}^\top\boldsymbol{\sigma}dV - \int_{\mathscr{V}} \mathbf{u}^\top\mathbf{b}dV - \mathbf{q}^\top\mathbf{p} - \int_{\partial\mathscr{V}} \mathbf{u}^\top\mathbf{t}_\mathrm{S}dS - \int_{\mathscr{V}} \rho\ddot{\mathbf{u}}^\top\mathbf{u}dV \\ &= \frac{1}{2}\int_{\mathscr{V}} \mathbf{q}^\top\mathbf{B}^\top\mathbf{D}\mathbf{B}\mathbf{q}dV - \int_{\mathscr{V}} \mathbf{q}^\top\mathbf{S}^\top\mathbf{b}dV - \mathbf{q}^\top\mathbf{p} - \int_{\partial\mathscr{V}} \mathbf{q}^\top\mathbf{S}_\mathrm{S}{}^\top\mathbf{t}_\mathrm{S}dS \\ &\quad - \int_{\mathscr{V}} \rho\ddot{\mathbf{q}}^\top\mathbf{S}^\top\mathbf{S}\mathbf{q}dV, \end{aligned} \tag{15}$$

where U is the strain energy; W_b is the potential body forces work; W_p is the potential concentrated loads work; W_s is the potential distributed loads work; W_I is the potential inertial force work; $\mathbf{b}$ is the body weight density matrix; $\mathbf{p}$ is the concentrated external loads applied at the nodes; $\mathbf{t}_\mathrm{S}$ is the surface load, and $\mathbf{S}_\mathrm{S}$ is the shape function matrix evaluated along the surface; ρ is the density of an element, and $\ddot{\mathbf{q}}$ is the second derivative of $\mathbf{q}$ with respect to time. Based on the principle of virtual work (i.e., $\delta\Pi = 0$), the FEM dynamic equation is written as:

$$\mathbf{M}\ddot{\mathbf{q}} + \mathbf{K}\mathbf{q} = \mathbf{F}, \tag{16}$$

where both $\mathbf{M}$, $\mathbf{K}$, and $\mathbf{F}$ arise from the summation of all elements, i.e.,

$$\mathbf{M} = \sum_e \mathbf{T}_e{}^\top\mathbf{M}^{(e)}\mathbf{T}_e, \tag{17}$$

$$\mathbf{K} = \sum_e \mathbf{T}_e^\top\mathbf{K}^{(e)}\mathbf{T}_e, \tag{18}$$

$$\mathbf{F} = \mathbf{p} + \sum_e \mathbf{T}_e^\top\mathbf{F}^{(e)}. \tag{19}$$

The local mass matrix $\mathbf{M}^{(e)}$, local stiffness matrix $\mathbf{K}^{(e)}$, and local volumetric and surface force vector $\mathbf{F}^{(e)}$ is written as:

$$\mathbf{M}^{(e)} = \int_{\mathscr{V}^{(e)}} \rho\mathbf{S}^\top\mathbf{S}dV, \tag{20}$$

$$\mathbf{K}^{(e)} = \int_{\mathscr{V}^{(e)}} \mathbf{B}^\top\mathbf{D}\mathbf{B}dV, \tag{21}$$

$$\mathbf{F}^{(e)} = \int_{\mathscr{V}^{(e)}} \mathbf{S}^\top\mathbf{b}dV + \int_{\partial\mathscr{V}^{(e)}} \mathbf{S}_\mathrm{S}{}^\top\mathbf{t}_\mathrm{S}dS, \tag{22}$$

$$\mathscr{V}^{(e)} = tA_e = t\left(A_\mathrm{f} + A_\mathrm{m}\right), \tag{23}$$

where $\mathscr{V}^{(e)}$ and $\partial\mathscr{V}^{(e)}$ are the element volume and surface regions where external load exists; t is the element thickness, A_f, A_m, and A_e are areas of fiber, matrix, and the entire element. From modal analysis, the kth mode satisfies

$$\left(\mathbf{K} - \omega_k^2\mathbf{M}\right)\boldsymbol{\Psi}_k = 0, \tag{24}$$

where ω_k and $\boldsymbol{\Psi}_k$ are the corresponding natural frequency and mode shape. For static analysis, the inertial term in Eq. (16) is zero, and FEM is reduced to the following form:

$$\mathbf{K}\mathbf{U} = \mathbf{F}, \tag{25}$$

The static form is mostly exploited in the following compliance analysis and fiber path optimization.

2.2. B-spline-based fiber path reinforcement contribution

2.2.1. B-spline parameterization of fiber path

Though the conventional FEM formulations can be easily calculated, the elastic and mass matrices in the fiber-reinforced region require the area of the fiber A_f and the orientation of fiber θ. To calculate these parameters, the fiber paths need to be represented mathematically, but this representation is challenging for optimization since it has infinite degrees of freedom. The B-spline provides a compact and shape-preserving representation of a curve, effectively reducing the degrees of freedom compared to direct sampling. Manipulating a limited portion by the control points does not affect the overall shape of the curve, increasing the flexibility of the represented paths. Moreover, the convex hull of the control points envelops and subdivides the B-spline into segments, yielding a local geometric interpretation for the fiber paths. The standard B-spline is given by

$$\mathbf{c}(\xi) = \sum_{\zeta=1}^{n_\mathrm{c}} N_{\zeta,m}(\xi)\mathbf{p}_{\mathrm{c},\zeta}, \tag{26}$$

where $\xi \in [0,1]$ is the B-spline curve parameter, n_c is the number of control points, $\mathbf{p}_{\mathrm{c},\zeta}$ is the ζth control point, and $N_{\zeta,m}(\xi)$ is the ζth normalized m-order B-spline basis function defined as:

$$N_{\zeta,1}(\xi) = \begin{cases} 1, & \xi_\zeta \leqslant \xi < \xi_{\zeta+1} \\ 0, & \text{otherwise} \end{cases}, \tag{27}$$

$$N_{\zeta,m}(\xi) = \frac{(\xi - \xi_\zeta)N_{\zeta,m-1}(\xi)}{\xi_{\zeta+m-1} - \xi_\zeta} + \frac{(\xi_{\zeta+m} - \xi)N_{\zeta+1,m-1}(\xi)}{\xi_{\zeta+m} - \xi_{\zeta+1}}. \tag{28}$$

Note that ξ_i is the knot in a non-decreasing sequence of real number $\{\xi_1, \cdots, \xi_{n_\mathrm{c}+m}\}$ called knot vector. Assume there are N_f continuous fibers inside the reinforced region, the ith continuous fiber is represented by a m-order B-spline with $n_\mathrm{c}^{(i)}$ control points $\mathbf{p}_{\mathrm{c},1}^{(i)}, \mathbf{p}_{\mathrm{c},2}^{(i)}, \ldots, \mathbf{p}_{\mathrm{c},n_\mathrm{c}^{(i)}}^{(i)}$, where each control points $\mathbf{p}_{\mathrm{c},\zeta}^{(i)} \in \mathbb{R}^2$. These control points are concatenated to a control point matrix $\mathbf{P}_{\mathrm{c}}^{(i)} \in \mathbb{R}^{n_{\mathrm{c}}^{(i)} \times 2}$ given by:

$$\mathbf{P}_{\mathrm{c}}^{(i)} = \left[\mathbf{p}_{\mathrm{c},1}^{(i)} \quad \mathbf{p}_{\mathrm{c},2}^{(i)} \quad \cdots \quad \mathbf{p}_{\mathrm{c},n_{\mathrm{c}}^{(i)}}^{(i)} \right]^{\top}. \tag{29}$$

The ith continuous fiber is thus given by:

$$\mathbf{c}^{(i)}\left(\xi, \mathbf{P}_{\mathrm{c}}^{(i)}\right) = \mathbf{N}^{(i)}(\xi)\mathbf{P}_{\mathrm{c}}^{(i)}, \tag{30}$$

where $\mathbf{N}^{(i)}(\xi)$ is the vector combination of the set of basis functions of the ith B-spline. Without loss of generality, all the B-spline parameterizations are assumed to have the same order and knot spacing. Therefore, the basis functions are identical for the same number of control points and knot vector, i.e., $\mathbf{N}^{(i)}(\xi) = \mathbf{N}^{(j)}(\xi)$ if $n_{\mathrm{c}}^{(i)} = n_{\mathrm{c}}^{(j)}$. Without loss of generality, the fiber element intersection relationship applies to all fiber paths. Therefore, the superscript $^{(i)}$ is omitted in Sections 2.2.2 and 2.2.3 to reduce equation complexity.

2.2.2. Probability-enabled stiffness and mass matrix calculation

In the current framework, following Eqs. (20) and (21), the fiber path affects the stiffness and mass matrix via the orientation and areas inside an element. These quantities typically require calculating the intersection points of the fiber path and each element [35]. Since the mesh's characteristic size is assumed to be significantly smaller than the fiber's achievable radius of curvature, the orientation inside an element can be represented by an average value $\overline{\theta}$ to simplify the calculation, as shown in Fig. 2(c). With this assumption, the stiffness matrix in Eq. (21) is simplified to

$$\begin{aligned} &\mathbf{K}^{(e)} = tA_{\mathrm{f}}\mathbf{B}^{\top}\mathbf{D}_{\mathrm{f}}\mathbf{B} + tA_{\mathrm{m}}\mathbf{B}^{\top}\mathbf{D}_{\mathrm{m}}\mathbf{B}, \\ &\mathbf{D}_{\mathrm{f}} = \mathbf{T}\left(\overline{\theta}\right)^{\top}\mathbf{D}_{\mathrm{f0}}\mathbf{T}\left(\overline{\theta}\right). \end{aligned} \tag{31}$$

Accordingly, the change of the local stiffness matrix when the fiber path intersects is given by:

$$\Delta\mathbf{K}^{(e)} = twL_{\mathrm{f}}\mathbf{B}^{\top}\left(\mathbf{D}_{\mathrm{f}} - \mathbf{D}_{\mathrm{m}}\right)\mathbf{B}, \tag{32}$$

where w is the width of fiber, L_{f} is the length of fiber in an element. Similarly, the mass matrix in Eq. (20) is simplified to:

$$\mathbf{M}^{(e)} = tA_{\mathrm{f}}\rho_{\mathrm{f}}\mathbf{S}^{\top}\mathbf{S} + tA_{\mathrm{m}}\rho_{\mathrm{m}}\mathbf{S}^{\top}\mathbf{S}, \tag{33}$$

$$\Delta\mathbf{M}^{(e)} = tA_{\mathrm{f}}\left(\rho_{\mathrm{f}} - \rho_{\mathrm{m}}\right)\mathbf{S}^{\top}\mathbf{S} = twL_{\mathrm{f}}\left(\rho_{\mathrm{f}} - \rho_{\mathrm{m}}\right)\mathbf{S}^{\top}\mathbf{S}, \tag{34}$$

where ρ_{f} and ρ_{m} are the density of fiber and matrix material. The two terms L_{f} and $\overline{\theta}$ are key to the changes in the mass and stiffness matrices, and their semi-analytical relationships with the control points need to be established to establish the gradients of FEM.

Accurate calculations of the intersection points are usually time-consuming and create numerical singularities, hindering efficient optimization. Moreover, the realistic fiber width and curvature introduce errors to the simplified geometrical calculation. Therefore, this section establishes a semi-analytical fiber-in-element probability (AFEP) function describing the intersection relationship between the element and the fiber under a probability framework. This framework enables efficient computation accounting for limited fiber width's contributions to the FEM, as well as its gradients to the fiber path control points. A probability function is introduced instead of accurately calculating the intersection point of the fiber path and the element.

Consider a polygon with N_{p} clockwise vertexes $\mathbf{p}_1, \mathbf{p}_2, \cdots, \mathbf{p}_{N_{\mathrm{p}}}$. A criterion of an arbitrary point $\mathbf{c}$ inside the polygon is determined with the following cross-product conditions:

$$(\mathbf{c} - \mathbf{p}_{\mathrm{k}}) \times (\mathbf{p}_{k+1} - \mathbf{p}_{\mathrm{k}}) > 0, \ k = 1, 2, \cdots, N_{\mathrm{p}} \tag{35}$$

where $\mathbf{p}_{N_{\mathrm{p}}+1} = \mathbf{p}_1$. These binary criteria shed light on determining fiber and element intersections, which is crucial to fiber path optimization. Combining these binary relationships in Eq. (35) to a single probability function, the AFEP is defined as:

$$\psi\left(\mathbf{c}, \mathbf{p}_1, \mathbf{p}_2, \cdots, \mathbf{p}_{N_{\mathrm{p}}}\right) = \prod_{k=1}^{N_{\mathrm{p}}} \sigma_{\mathrm{sig}}\left(\frac{(\mathbf{c} - \mathbf{p}_k) \times (\mathbf{p}_{k+1} - \mathbf{p}_k)}{w\|\mathbf{p}_{k+1} - \mathbf{p}_k\|}\right), \tag{36}$$

where $\psi\left(\mathbf{c}, \mathbf{p}_1, \mathbf{p}_2, \cdots, \mathbf{p}_{N_{\mathrm{p}}}\right)$ approximate the probability of arbitrary point $\mathbf{c}$ inside the polygon with vertexes given by $\mathbf{p}_1, \mathbf{p}_2, \cdots, \mathbf{p}_{N_{\mathrm{p}}}$. The binary relationships are replaced by the multiplication of the sigmoid function σ_{sig} to indicate probability. The sigmoid function is defined as:

$$\sigma_{\mathrm{sig}}(x) = \frac{1}{1 + e^{-x}}. \tag{37}$$

Note that σ_{sig} equals to one and zero as it tends towards positive and negative infinity, respectively. This property, along with the normalization with the edge length $\|\mathbf{p}_{k+1} - \mathbf{p}_k\|$ and the fiber width w, ensures that $\psi = 1$ when the point $\mathbf{c}$ is at least half-width from the boundary, and $\psi = 0.5$ when the point $\mathbf{c}$ sits on the boundary of the polygon. This continuous probability agrees with the physical fiber and element intersection area (as shown in Fig. 3), thus enhancing the fiber optimization's smoothness. The continuity of the AFEP function is further illustrated by a case showing the change in local fiber length L_{f} and stiffness increment $\left\|\Delta\mathbf{K}^{(e)}\right\|$ when the fiber path moving through elements. The movement of the fiber path is represented by the displacement percentage D_p illustrated with the red arrow shown in Fig. 4(a). The swept triangular elements are numbered, and these elements' corresponding fiber length and stiffness increment are plotted in Fig. 4(b). In addition, the gradients of these two variables are provided to illustrate the continuity of the AFEP function.

With this AFEP function, the intersection region of the B-spline and a triangular element no longer needs explicit intersection point evaluation. For a set of given control points, the B-spline curve length function $l(\xi, \mathbf{P}_{\mathrm{c}})$ is given by:

$$l(\xi, \mathbf{P}_{\mathrm{c}}) = \int_0^{\xi} \sqrt{\mathbf{P}_{\mathrm{c}}{}^{\top}\mathbf{N}\prime(\nu)^{\top}\mathbf{N}\prime(\nu)\mathbf{P}_{\mathrm{c}}}\,d\nu, \tag{38}$$

where $\mathbf{N}\prime(\xi) = d\mathbf{N}(\xi)/d\xi$ is the derivative of the basis function. The length of fiber inside the eth element L_{f} is given by:

$$L_{\mathrm{f}} = \int_0^1 \psi\left(\mathbf{c}(\xi, \mathbf{P}_{\mathrm{c}}), \mathbf{p}_1^{(e)}, \mathbf{p}_2^{(e)}, \mathbf{p}_3^{(e)}\right)\underbrace{\frac{\partial l(\xi, \mathbf{P}_{\mathrm{c}})}{\partial \xi}d\xi}_{dl}. \tag{39}$$

From the integral format of $l(\xi, \mathbf{P}_{\mathrm{c}})$ in Eq. (38), the derivative of curve length is given by:

$$\frac{\partial l(\xi, \mathbf{P}_{\mathrm{c}})}{\partial \xi} = \sqrt{\mathbf{P}_{\mathrm{c}}{}^{\top}\mathbf{N}\prime(\xi)^{\top}\mathbf{N}\prime(\xi)\mathbf{P}_{\mathrm{c}}}. \tag{40}$$

The vector approximating the connection between the entry and the exiting points is given by:

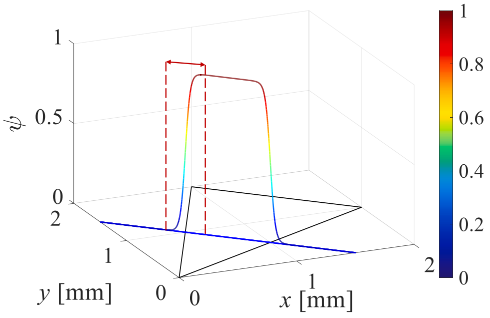

Fig. 3. Identification of a fiber path in an element by AFEP function.

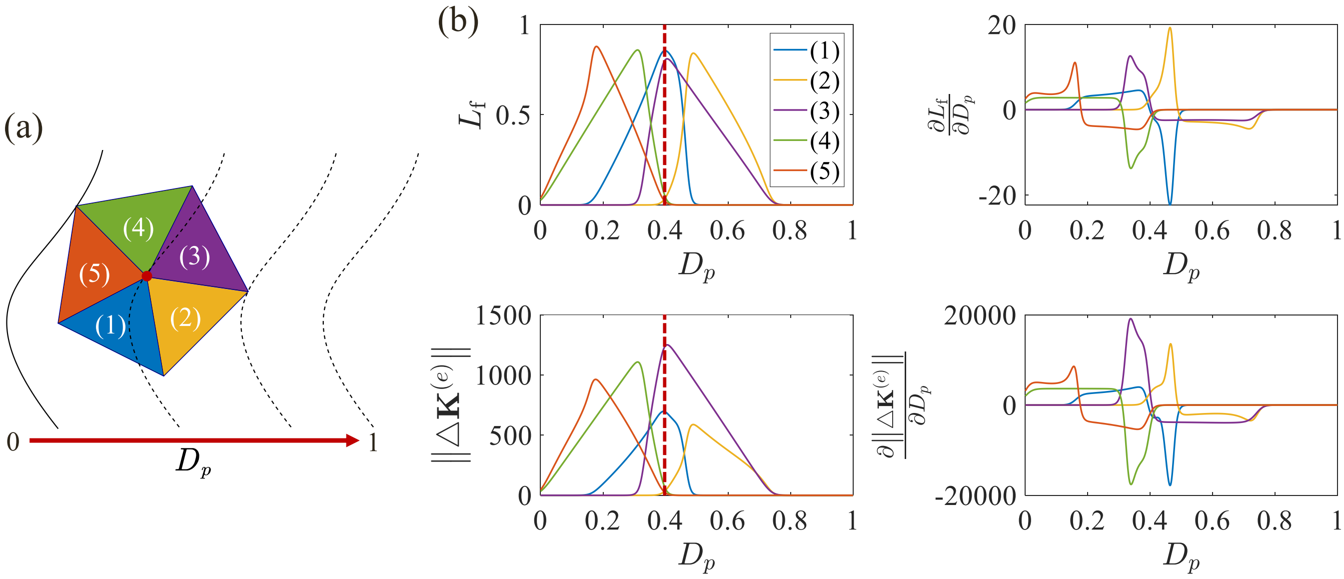

Fig. 4. A case of fiber path moving through elements with (a) schematic plot, (b) the changes of local fiber length and stiffness increment with the gradients of the changes.

$$\mathbf{z} = \int_0^1 \psi\left(\mathbf{c}(\xi, \mathbf{P}_c), \mathbf{p}_1^{(e)}, \mathbf{p}_2^{(e)}, \mathbf{p}_3^{(e)}\right) \mathbf{N}\prime(\xi) \mathbf{P}_c d\xi. \tag{41}$$

This vector $\mathbf{z} = [z_x, z_y]$ defines the average fiber direction inside this element, and thus is given by:

$$\overline{\theta} = \arctan(z_y/z_x). \tag{42}$$

Accordingly, the two critical variables describe the fiber and element relationship, L_f and $\overline{\theta}$, are determined without explicit calculation of the intersection points. Inserting these two values into Eqs. (32) and (34) enables the calculation of the fiber-reinforced elements.

2.2.3. *Convex-hull enabled calculation simplification*

Although Eq. (39) and (42) provides a way to calculate the critical terms L_f, $\overline{\theta}$, and their gradients, the calculation requires the AFEP of all elements, which is not computationally efficient. The B-spline convex hull property enables a preliminary selection of the elements that may interest the fiber, and thus significantly reduces the computational complexity. For a m-order B-spline with n_c control points, the fiber path can be decomposed into $n_c - m + 1$ segments. The jth segments defined with the curve parameter $\xi \in \left[\xi_{j+m-1}, \xi_{j+m}\right]$ is merely affected by m neighborhood control points defined as:

$$\mathbf{P}_c^{[j]} = \left[\mathbf{p}_{c,j}, \mathbf{p}_{c,j+1}, \cdots, \mathbf{p}_{c,j+m-1}\right]^{\top}. \tag{43}$$

More specifically, these segments are confined with the convex hull of $\mathbf{P}_c^{[j]}$, defined as $\mathscr{C}_{\mathbf{P}_c^{[j]}}$. Here, the set of elements that intersect with $\mathscr{C}_{\mathbf{P}_c^{[j]}}$ can be efficiently identified. This is achieved by two steps: (i) find all nodes within $\mathbf{P}_c^{[j]}$ and their related elements $\mathscr{T}_1^{[j]}$, and (ii) find the elements that contain the vertices of $\mathbf{P}_c^{[j]}$, defined as $\mathscr{T}_2^{[j]}$. The set of elements with potential intersections is given by:

$$\mathscr{T}^{[j]} = \mathscr{T}_1^{[j]} \cup \mathscr{T}_2^{[j]}. \tag{44}$$

This selection is no longer a probabilistic relationship, and thus the criteria of an arbitrary point $\mathbf{c}$ inside a polygon given by Eq. (35) is modified as:

$$\frac{(\mathbf{c} - \mathbf{p}_k) \times (\mathbf{p}_{k+1} - \mathbf{p}_k)}{\|\mathbf{p}_{k+1} - \mathbf{p}_k\|} > -w, \; k = 1, 2, \cdots. \tag{45}$$

This modification guarantees that the fiber width's contribution is considered in finding $\mathscr{T}^{[j]}$. Note that the jth segments only affect the elements in $\mathscr{T}^{[j]}$. This leads to a simplification of the Eqs. (39) and (41), given by:

$$L_f = \begin{cases} \displaystyle\int_{\xi_{j+m-1}}^{\xi_{j+m}} \psi \frac{\partial l(\xi, \mathbf{P}_c)}{\partial \xi} d\xi, & \text{when } e \in \mathscr{T}^{[j]} \\ 0, & \text{when } e \notin \mathscr{T}^{[j]} \end{cases}, \tag{46}$$

$$\mathbf{z} = \begin{cases} \displaystyle\int_{\xi_{j+m-1}}^{\xi_{j+m}} \psi \mathbf{N}\prime(\xi) \mathbf{P}_c d\xi, & \text{when } e \in \mathscr{T}^{[j]} \\ 0, & \text{when } e \notin \mathscr{T}^{[j]} \end{cases}. \tag{47}$$

With this convex-hull-enabled calculation of the local stiffness and mass matrix, the overall FEM-BFP method is summarized in a pseudo algorithm shown in Table 1.

3. Gradient-based B-spline fiber path optimization

3.1. *Semi-analytical gradients concerning the B-spline control points*

Gradients are crucial in optimization algorithms since they can enhance the optimization efficiency and speed. In the current FEM-BFP framework with semi-analytical expressions, the stiffness and mass matrix gradients with respect to the B-spline control points can also be conveniently constructed in Section 3.1.1. To enable desirable fiber-to-fiber distancing, a semi-analytical potential function with its gradients is also derived in Section 3.1.2.

3.1.1. *Semi-analytical gradients of FEM-BFP*

According to the simplification method in Section 2.2.3, the control points $\mathbf{P}_c^{[j]}$ of jth convex hull are a part of $\mathbf{P}_c$; the relationship is specified by a selector matrix $\mathbf{T}_j$ as:

$$\mathbf{P}_c^{[j]} = \mathbf{T}_j \mathbf{P}_c, \tag{48}$$

The gradient of the stiffness matrix increments (defined in Eq. (32)) with respect to the local control points $\mathbf{P}_c^{[j]}$ is given by:

$$\frac{\partial \Delta \mathbf{K}^{(e)}}{\partial \mathbf{P}_c^{[j]}} = tw\left[\frac{\partial L_f}{\partial \mathbf{P}_c^{[j]}} \mathbf{B}^{\top} (\mathbf{D}_f - \mathbf{D}_m) \mathbf{B} + L_f \mathbf{B}^{\top} \frac{\partial \mathbf{D}_f}{\partial \mathbf{P}_c^{[j]}} \mathbf{B}\right], \tag{49}$$

Table 1
FEM-BFP method's pseudo algorithm.

```
Input: geometry data, mesh data, fiber data, material properties, boundary conditions
Output: $\mathbf{K}$, $\mathbf{M}$, $\mathbf{F}$, $\mathbf{U}$
Main:
    // Generate homogeneous part's stiffness and mass matrices
    $\mathbf{K} = \mathrm{FEM.ASSEMBLE}(\mathbf{K}^{(e)})$
    $\mathbf{M} = \mathrm{FEM.ASSEMBLE}(\mathbf{M}^{(e)})$
    // Summation of the fiber reinforcement contribution
    for $i = 1 : N_\mathrm{f}$ do
        for $j = 1 : n_\mathrm{c} - m + 1$ do
            $\mathbf{P}_\mathrm{c}^{[j]} = \mathbf{P}_\mathrm{c}^{(i)}(j : j + m - 1)$
            $\xi \in [\xi_{j+m-1},\ \xi_{j+m}]$
            $\mathcal{C}_{\mathbf{P}_\mathrm{c}^{[j]}} = \mathrm{ConvexHull.CREATE}(\mathbf{P}_\mathrm{c}^{[j]})$
            $\mathcal{T}_1^{[j]} = \mathrm{Mesh.MAP}\left(\mathrm{ConvexHull.INSIDE}\left(\mathcal{C}_{\mathbf{P}_\mathrm{c}^{[j]}},\ \{node\}\right)\right)$
            $\mathcal{T}_2^{[j]} = \mathrm{Mesh.MAP}\left(\mathrm{ConvexHull.VERTICES}\left(\mathcal{C}_{\mathbf{P}_\mathrm{c}^{[j]}}\right)\right)$
            $\mathcal{T}^{[j]} = \mathcal{T}_1^{[j]} \cup \mathcal{T}_2^{[j]}$
            for $element \in \mathcal{T}^{[j]}$ do
                $[L_\mathrm{f},\ \mathbf{z}] = \mathrm{INTEGRATION}(\psi,\ \mathrm{Mesh.VERTICES}(element),\ \xi,\ \mathbf{N}',\ \mathbf{P}_\mathrm{c})$
                $\bar{\theta} = \arctan(\mathbf{z})$
                $\Delta\mathbf{K}^{(e)} = twL_\mathrm{f}\mathbf{B}^\top\left(\mathbf{D}_\mathrm{f}\left(\bar{\theta}\right) - \mathbf{D}_\mathrm{m}\right)\mathbf{B}$
                $\Delta\mathbf{M}^{(e)} = twL_\mathrm{f}(\rho_\mathrm{f} - \rho_\mathrm{m})\mathbf{S}^\top\mathbf{S}$
                $\mathbf{K} = \mathbf{K} + \mathrm{FEM.ASSEMBLE}(\Delta\mathbf{K}^{(e)})$
                $\mathbf{M} = \mathbf{M} + \mathrm{FEM.ASSEMBLE}(\Delta\mathbf{M}^{(e)})$
            end for
        end for
    end for
    // Solution of FEM
    $[\mathbf{U},\ \mathbf{F}] = \mathrm{FEM.STATIC}(\mathbf{K},\ boundary\ conditions)$
```

and the gradient to all control points is specified by:

$$\frac{\partial \Delta \mathbf{K}^{(e)}}{\partial \mathbf{P}_{\mathrm{c}}} = \sum_{j=1}^{n_{\mathrm{c}}-m+1} \frac{\partial \Delta \mathbf{K}^{(e)}}{\partial \mathbf{P}_{\mathrm{c}}^{[j]}} \mathbf{T}_j. \tag{50}$$

Similarly, the gradient of the mass matrix is given by:

$$\begin{aligned} \frac{\partial \Delta \mathbf{M}^{(e)}}{\partial \mathbf{P}_{\mathrm{c}}^{[j]}} &= tw \frac{\partial L_{\mathrm{f}}}{\partial \mathbf{P}_{\mathrm{c}}^{[j]}} (\rho_{\mathrm{f}} - \rho_{\mathrm{m}}) \mathbf{S}^{\top} \mathbf{S}, \\ \frac{\partial \Delta \mathbf{M}^{(e)}}{\partial \mathbf{P}_{\mathrm{c}}} &= \sum_{j=1}^{n_{\mathrm{c}}-m+1} \frac{\partial \Delta \mathbf{M}^{(e)}}{\partial \mathbf{P}_{\mathrm{c}}^{[j]}} \mathbf{T}_j. \end{aligned} \tag{51}$$

Without loss of generality, the gradient applies to all convex hulls. Therefore, the superscript $^{[j]}$ is omitted in this section to reduce equation complexity. The two partial derivatives $\partial L_{\mathrm{f}}/\partial \mathbf{P}_{\mathrm{c}}$ and $\partial \mathbf{D}_{\mathrm{f}}/\partial \mathbf{P}_{\mathrm{c}}$ are derived from Eqs. (39) and (46) as:

$$\frac{\partial L_{\mathrm{f}}}{\partial \mathbf{P}_{\mathrm{c}}} = \int_{\xi_{j+m-1}}^{\xi_{j+m}} \left(\frac{\partial \psi}{\partial \mathbf{c}} \frac{\partial \mathbf{c}}{\partial \mathbf{P}_{\mathrm{c}}} \frac{\partial l}{\partial \xi} + \psi \frac{\partial^2 l}{\partial \xi \partial \mathbf{P}_{\mathrm{c}}} \right) d\xi. \tag{52}$$

The introduction of the continuous AFEP function enables the convenient calculation of the term $\partial \psi / \partial \mathbf{c}$. Along with Eq. (40), the first term in Eq. (52) is given by:

$$\frac{\partial \psi}{\partial \mathbf{c}} \frac{\partial \mathbf{c}}{\partial \mathbf{P}_{\mathrm{c}}} \frac{\partial l}{\partial \xi} = \frac{\partial \psi}{\partial \mathbf{c}} \mathbf{N} \sqrt{\mathbf{P}_{\mathrm{c}}{}^{\top} \mathbf{N}'(\xi)^{\top} \mathbf{N}'(\xi) \mathbf{P}_{\mathrm{c}}}, \tag{53}$$

while the second term is given by:

$$\psi \frac{\partial^2 l}{\partial \xi \partial \mathbf{P}_{\mathrm{c}}} = \psi \frac{\mathbf{N}'(\xi)^{\top} \mathbf{N}'(\xi) \mathbf{P}_{\mathrm{c}}}{\sqrt{\mathbf{P}_{\mathrm{c}}{}^{\top} \mathbf{N}'(\xi)^{\top} \mathbf{N}'(\xi) \mathbf{P}_{\mathrm{c}}}}. \tag{54}$$

Apart from the term $\partial L_{\mathrm{f}}/\partial \mathbf{P}_{\mathrm{c}}$, the term $\partial \mathbf{D}_{\mathrm{f}}/\partial \mathbf{P}_{\mathrm{c}}$ is calculated with the chain rule:

$$\frac{\partial \mathbf{D}_{\mathrm{f}}}{\partial \mathbf{P}_{\mathrm{c}}} = \frac{\partial \mathbf{D}_{\mathrm{f}}}{\partial \mathbf{T}} \frac{\partial \mathbf{T}}{\partial \overline{\theta}} \frac{\partial \overline{\theta}}{\partial \mathbf{P}_{\mathrm{c}}}. \tag{55}$$

Due to the definition of $\mathbf{D}_{\mathrm{f}}$ in Eq. (31) and $\mathbf{D}_{\mathrm{f0}}$ in Eq. (12), the first two terms are conveniently calculated as:

$$\frac{\partial \mathbf{D}_{\mathrm{f}}}{\partial \mathbf{T}} = 2\mathbf{D}_{\mathrm{f0}} \mathbf{T}, \tag{56}$$

$$\frac{\partial \mathbf{T}}{\partial \overline{\theta}} = \begin{bmatrix} -2\cos\overline{\theta}\sin\overline{\theta} & 2\cos\overline{\theta}\sin\overline{\theta} & 2\cos^2\overline{\theta} - 2\sin^2\overline{\theta} \\ 2\cos\overline{\theta}\sin\overline{\theta} & -2\cos\overline{\theta}\sin\overline{\theta} & 2\sin^2\overline{\theta} - 2\cos^2\overline{\theta} \\ \sin^2\overline{\theta} - \cos^2\overline{\theta} & \cos^2\overline{\theta} - \sin^2\overline{\theta} & -4\cos\overline{\theta}\sin\overline{\theta} \end{bmatrix}. \tag{57}$$

The gradient of the direction is given by:

$$\frac{\partial \overline{\theta}}{\partial \mathbf{P}_{\mathrm{c}}} = \frac{\partial \overline{\theta}}{\partial \mathbf{z}} \frac{\partial \mathbf{z}}{\partial \mathbf{P}_{\mathrm{c}}}, \tag{58}$$

where,

$$\frac{\partial \overline{\theta}}{\partial \mathbf{z}} = \left[\frac{-z_y}{z_x^2 + z_y^2}, \frac{z_x}{z_x^2 + z_y^2} \right], \tag{59}$$

$$\frac{\partial \mathbf{z}}{\partial \mathbf{P}_{\mathrm{c}}} = \int_{\xi_{j+m-1}}^{\xi_{j+m}} \left(\frac{\partial \psi}{\partial \mathbf{c}} \frac{\partial \mathbf{c}}{\partial \mathbf{P}_{\mathrm{c}}} \mathbf{N}'(u) \mathbf{P}_{\mathrm{c}} + \psi \mathbf{N}'(u) \right) d\xi. \tag{60}$$

With these semi-analytical gradients defined in Eqs. (49) to (60), the mass and stiffness matrix increments' gradients with respect to the fiber control points are established.

3.1.2. Fiber distancing control via a potential field

Except for the fiber path's contribution to the stiffness matrix, the manufacturing constraints also need to be considered in the optimization. The constraints include the distances between fibers and from the fiber to the part's boundary, which reserve sufficient space to avoid manufacturing defects like fiber overlapping and intersection. On the other hand, the distance between fibers needs to be reduced to enhance the local fiber density and achieve optimal reinforcement effect. Therefore, a potential field is introduced to the fibers, which provides an attraction at a far distance and a repulsion at a close distance. A potential (as illustrated in Fig. 5) is defined as:

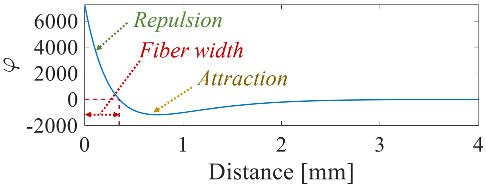

Fig. 5. The potential function for fiber distancing control.

$$\varphi = e^{-p_1 \left(\frac{r}{w_{\mathrm{p}}} - 1 \right)} - e^{-p_2 \left(\frac{r}{w_{\mathrm{p}}} - 1 - r_g \right)}, \tag{61}$$

where w_{p} is the reference width, p_1 represents the intensity of repulsion, p_2 represents the intensity of attraction, r is the distance between two points, and r_g is a dimensionless length parameter of the attraction region. Without loss of generality, the potential between the first two fiber paths with control points $\mathbf{P}_{\mathrm{c}}^{(1)}$ and $\mathbf{P}_{\mathrm{c}}^{(2)}$ is written as:

$$\phi = \int_0^1 \int_0^1 \varphi \left(r \left(\mathbf{P}_r \left(\xi^{(1)}, \xi^{(2)}, \mathbf{P}_{\mathrm{c}}^{(1)}, \mathbf{P}_{\mathrm{c}}^{(2)} \right) \right) \right) d\xi^{(1)} d\xi^{(2)}, \tag{62}$$

$$r = \left\| \mathbf{N}\left(\xi^{(1)}\right) \mathbf{P}_{\mathrm{c}}^{(1)} - \mathbf{N}\left(\xi^{(2)}\right) \mathbf{P}_{\mathrm{c}}^{(2)} \right\|, \tag{63}$$

$$\mathbf{P}_r = \left[\mathbf{N}\left(\xi^{(1)}\right) \mathbf{P}_{\mathrm{c}}^{(1)}, \mathbf{N}\left(\xi^{(2)}\right) \mathbf{P}_{\mathrm{c}}^{(2)} \right]^{\top}. \tag{64}$$

The relations apply to arbitrary two fibers in evaluating their distance. For the convenience of calculating the semi-analytical gradient, the control points are concatenated as:

$$\mathbf{P}_{\phi} = \left[\mathbf{P}_{\mathrm{c}}^{(1)}, \mathbf{P}_{\mathrm{c}}^{(2)} \right]^{\top}. \tag{65}$$

Then, the gradient of Eq. (62) is given by:

$$\frac{\partial \phi}{\partial \mathbf{P}_{\phi}} = \int_0^1 \int_0^1 \frac{\partial \varphi}{\partial r} \frac{\partial r}{\partial \mathbf{P}_r} \frac{\partial \mathbf{P}_r}{\partial \mathbf{P}_{\phi}} d\xi^{(1)} d\xi^{(2)}. \tag{66}$$

According to Eq. (61), the first term of Eq. (66) is given by:

$$\frac{\partial \varphi}{\partial r} = \frac{p_2}{w_{\mathrm{p}} e^{p_2 \left(\frac{r}{w_{\mathrm{p}}} - 1 \right)}} - \frac{p_1}{w_{\mathrm{p}} e^{p_1 \left(\frac{r}{w_{\mathrm{p}}} - 1 - r_g \right)}}. \tag{67}$$

The second term $\partial r / \partial \mathbf{P}_r$ in Eq. (66) is conveniently calculated according to the norm of the vector, while the third term is given by:

$$\frac{\partial \mathbf{P}_r}{\partial \mathbf{P}_{\phi}} = \begin{bmatrix} \mathbf{N}\left(\xi^{(1)}\right) & 0 \\ 0 & \mathbf{N}\left(\xi^{(2)}\right) \end{bmatrix}. \tag{68}$$

Similarly, a potential function solely providing repulsion is introduced between the fiber and the boundary defined as:

$$\varphi_{\mathrm{B}} = e^{-p_1 \left(\frac{r}{w_{\mathrm{b}}} - 1 \right)}, \tag{69}$$

where w_{b} is the reference width for boundary distancing. For a fiber path, the potential towards the boundary is written as:

$$\phi_{\mathrm{B}} = \int_{\partial \mathscr{V}} \int_0^1 \varphi \left(r \left(\mathbf{c}(\xi, \mathbf{P}_{\mathrm{c}}), \mathbf{p}_{\mathrm{B}} \right) \right) d\xi dS, \tag{70}$$

$$r = \left\| \mathbf{c} - \mathbf{p}_{\mathrm{B}} \right\|, \tag{71}$$

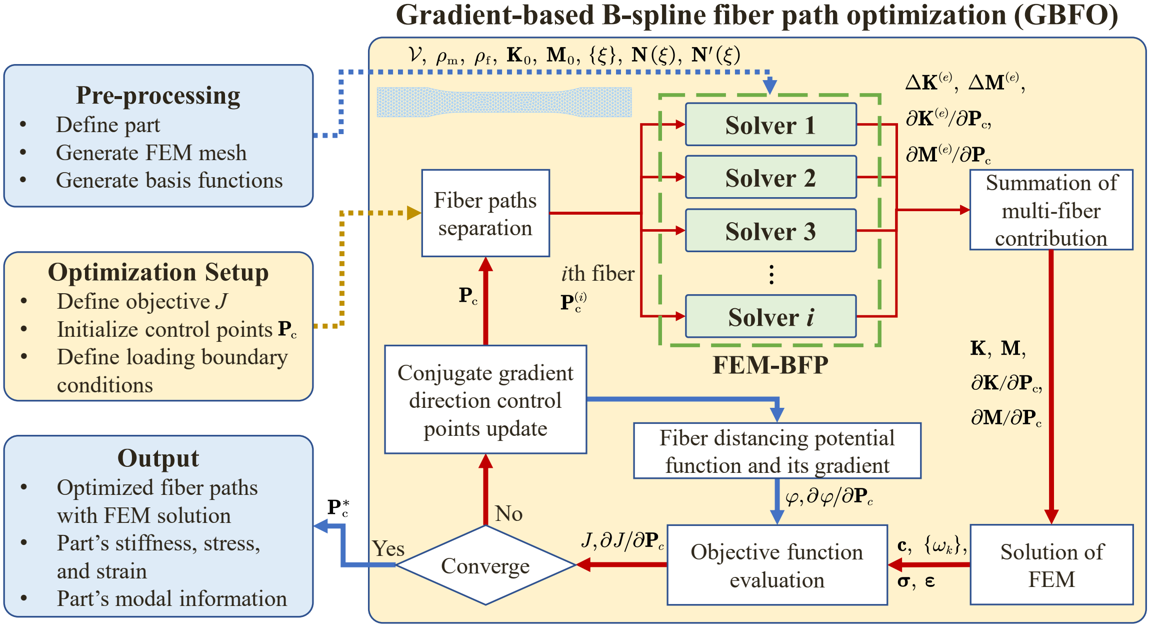

Fig. 6. The gradient-based B-spline fiber path optimization flow chart.

Table 2
The material parameters of fiber and matrix material.

Parameter	PLA	Continuous carbon fiber-reinforced thermoset polymer
Diameter [mm]	1.75	0.35
Density [g/cm^3]	1.25	1.51
Elastic modulus [MPa] (E_1)	2205.18	108,566.28
Elastic modulus [MPa] (E_2)	/	54,283.14
Tensile Strength [MPa]	49.8	2206
Poisson ratio	0.36	0.4

where $\mathbf{p}_B$ is a point on the part's boundary. Accordingly, the gradient is given by:

$$\frac{\partial \phi_B}{\partial \mathbf{P}_c} = \int_{\partial \mathscr{V}} \int_0^1 \frac{\partial \varphi}{\partial r} \frac{\partial r}{\partial \mathbf{c}} \frac{\partial \mathbf{c}}{\partial \mathbf{P}_c} d\xi dS, \tag{72}$$

where the first term is given by:

$$\frac{\partial \varphi}{\partial r} = -\frac{p_1}{w_b e^{p_1\left(\frac{r}{w_b}-1\right)}}. \tag{73}$$

The formula for $\partial r/\partial \mathbf{c}$ is the same as the term $\partial r/\partial \mathbf{P}_r$ in Eq. (66), and $\partial \mathbf{c}/\partial \mathbf{P}_c = \mathbf{N}$. With these potential functions, the fiber distancing control for fiber path optimization is established.

3.2. Optimization setup

The optimization of fiber paths aims to enhance the part's mechanical properties by manipulating the fiber's control points. The initial position of the control points is important for gradient-based optimization since the optimization can have a nonconvex problem, which leads to trapping in the local minimum. Considering the control points located in the low-stress region, the gradient of the stiffness matrix would have gentle slopes, and the tendency of fiber to move would be negligible. The initial position of the control points needs to appear near the high-stress region. There are several methods to generate the initial fiber paths. This paper uses a stress-based method called the principal stress direction method (PSD) [27,32] due to its straightforward fiber alignment to the load transfer region, improving computational efficiency. The overall optimization is defined as:

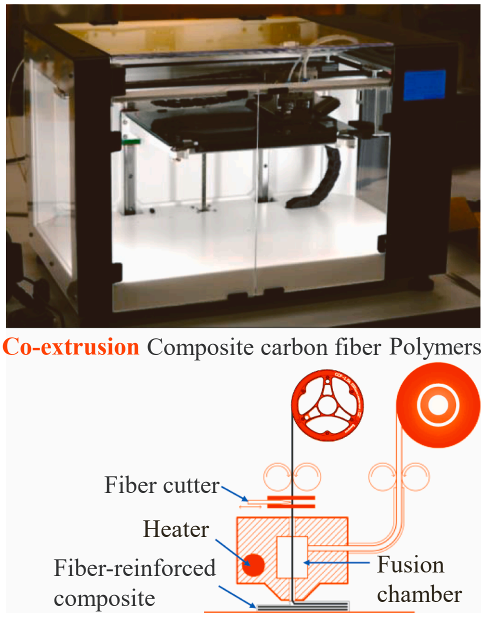

Fig. 7. Anisoprint composite A4 and co-extrusion illustration [36].

$$\left.\begin{aligned} &\min_{\mathbf{P}_c} J = \mu_1 c + \mu_2 L_f + \mu_3 f_\omega(\omega_k) \\ &\quad \text{subject to } \phi < \phi(w) \\ &\quad\quad \phi_B = 0 \end{aligned}\right\}, \tag{74}$$

where the major objectives are the total compliance $c = \mathbf{FU}$, the fiber length L_f, and the natural frequency ω_k of kth mode;μ_1, μ_2, and μ_3 are the optimization weight for each individual term, respectively. The function f_ω refers to a customized penalty function on the natural frequencies of the structure. Although the equations of $\mathbf{M}^{(e)}$ and $\partial\mathbf{M}^{(e)}/\partial\mathbf{P}_c$ are given, the natural frequency ω_k is obtained with the calculation of eigenvalue analysis, which could not provide a gradient formula. For those cases,

Table 3
The printing process parameters.

Nozzle temperature [°C]	Print speed [mm/s]	Matrix material layer thickness [mm]	Composite fiber layer thickness [mm]	Matrix material nozzle diameter [mm]	Composite fiber nozzle diameter [mm]
210	40	0.17	0.34	0.4	0.8

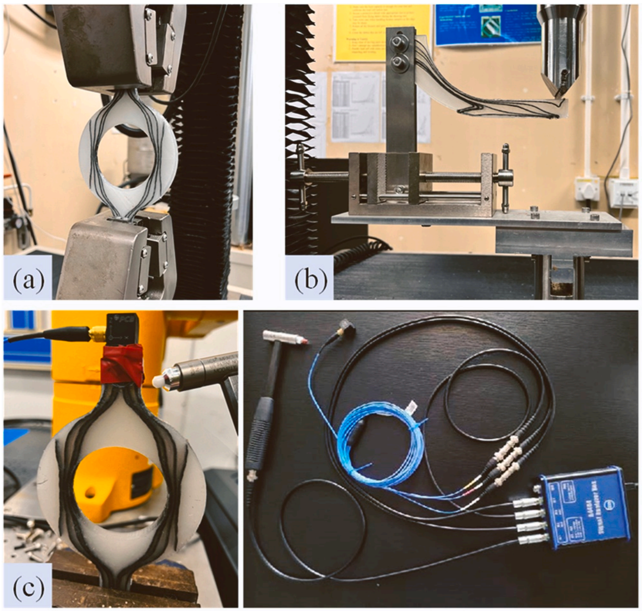

Fig. 8. The experiment platforms of (a) tensile test and (b) impact hammer modal test.

the numerical gradient of this frequency-related term can be exploited. Except for these objectives, note that the number of fibers in this optimization problem can be freely chosen. This could be achieved by setting the number of fibers N_f as an additional integer optimization variable, yielding a mixed-integer optimization problem. In a practical setting, tradeoff studies could determine the number of fibers with computationally efficient fiber path generation methods (e.g., principal stress direction method, etc.). The inter-fiber potential ϕ and the fiber-to-boundary potential ϕ_B are the manufacturing constraints to control the distance of printing toolpaths. Based on the FEM-BFP discussed in Section 2 and the gradient evaluation in Section 3, the optimization in Eq. (74) is conveniently solved via various optimization algorithms (e.g., Truncated-Newton algorithm, Conjugate gradient algorithm, Quasi-Newton algorithm, etc.). Since these algorithms are used for unconstrained optimization, ϕ and ϕ_B are added to the objectives as soft constraints for fiber distance control. The overall gradient-based B-spline fiber path optimization (GBFO) process is shown in Fig. 6. The process iteratively evaluates the objective function by implementing FEM-BFP. Each fiber path's contribution is solved and added to solve the mass and stiffness matrices, as well as their gradients. The objective function adds the solution and the constraints of fiber distancing potential. Once converged, the optimized control points $\mathbf{P}_c^*$ and the optimized part FEM information are outputted for manufacturing.

4. Simulation and experiment verification

4.1. Simulation and experiment platform

Both the proposed FEM-BFP and the GBFO run on a desktop computer with an 8-core R7–5800 H CPU. The matrix material and the continuous fiber are selected to be polylactic acid (PLA) and carbon fiber, respectively. Their mechanical properties are summarized in Table 2. The continuous-fiber-reinforced parts are fabricated by Anisoprint Composite A4 printer. This printer is based on a co-extrusion technology to realize the continuous fiber printing shown in Fig. 7. The slicing software AURA adjusts the printing speed, layer height, and temperature for fiber and PLA filaments with the process parameters shown in Table 3. Note that the layer thickness of the fiber is twice the thickness and the width of the matrix material. This arises from the geometry of the continuous fiber prepreg. The tensile and bending test is performed on the MTS Sintech 10/D universal test machine (Fig. 8(a), (b)) with a speed of 2 mm/s. The impact hammer modal tests are performed with the PCB356A17 accelerometer, the Model 086C03 impact hammer, and the Adash VA4 Pro vibration analyzer shown in Fig. 8(c).

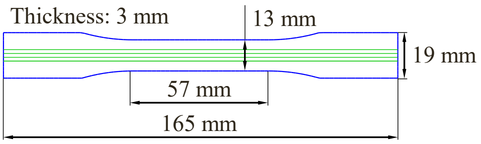

Fig. 9. The dumbbell-shaped tensile specimen with four fiber paths.

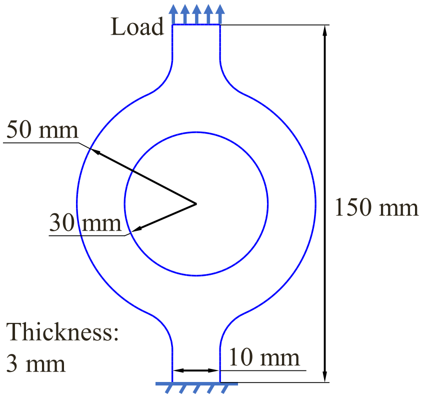

Fig. 10. The loop-shaped specimen and loading conditions.

Table 4
The comparison between FEM-BFP, Abaqus, and the tensile experiment of the dumbbell-shaped specimen.

	BFP-FEM	Abaqus	Experiment
Element number	1426	39,564	/
Stiffness [MPa]	13,581.05	13,043.04	13,120.99
Modeling error	3.51 %	0.59 %	/
Computation time [s]	7.8	14.1	/

4.2. FEM-BFP verification

To verify the FEM-BFP model, two representative specimens are designed and fabricated.

- The dumbbell-shaped specimen following ASTM D638 standard [37] with four fiber paths is shown in Fig. 9. The part is mainly for tensile testing to illustrate the accuracy of FEM-BFP.
- The loop-shaped specimen [27] and its representative loading conditions are shown in Fig. 10. The part is used to verify the modal response predictions of FEM-BFP in this section and further GBFO in Section 4.3.

The FEM-BFP is established in MATLAB with an open-source mesh generator named KMG [38]. The reference element edge length is 2 mm. The calculated stiffness is compared to a commercial software Abaqus

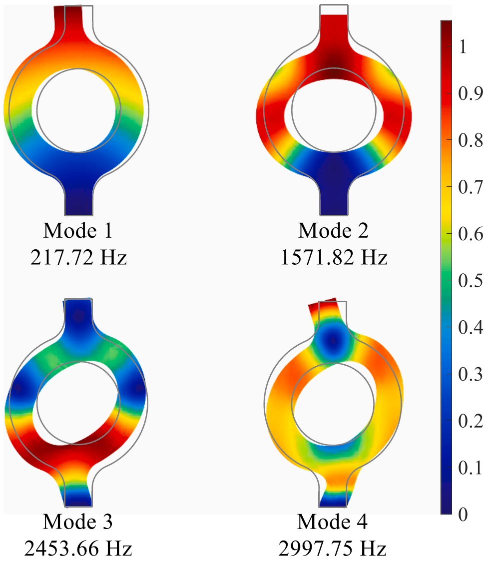

Fig. 11. First four mode shapes and natural frequencies of the loop-shaped part with FEM-BFP.

and the experimental MTS Sintech 10/D tensile test (shown in Fig. 8(a)).

The comparison results for the dumbbell-shaped specimen are detailed in Table 4. The proposed FEM-BFP method achieves similar levels of accuracy compared to the Abaqus simulations with significantly fewer elements. The number of elements in Abaqus is tuned to the point of convergence. The computational time of the FEM-BFP method is also less than the Abaqus method, while providing additional gradient information with respect to the fiber control points.

To verify the loop-shaped parts shown in Fig. 10, a set of fiber paths is created by the PSD method. The PSD method obtains a tensile stress field by selecting the principal stresses of elements since the fiber has higher stiffness and strength under tensile conditions than compression conditions [27]. Then, the stress field is filled by streamlines with aligned directions to the stress direction [32]. An open-source B-spline conversion toolbox converts the streamlines into control points. The uniform knot vector is defined before the conversion, determining the number of control points to ensure sufficient degrees of freedom and computational efficiency. The position of the control points is also determined based on the shape of the streamline and the knot vector.

In the modal analysis, the calculated natural frequencies and mode shapes are shown in Fig. 11. To acquire these mode shapes, impact hammer modal tests with different impact locations, directions, and accelerometer installation directions are performed, as shown in Fig. 12.

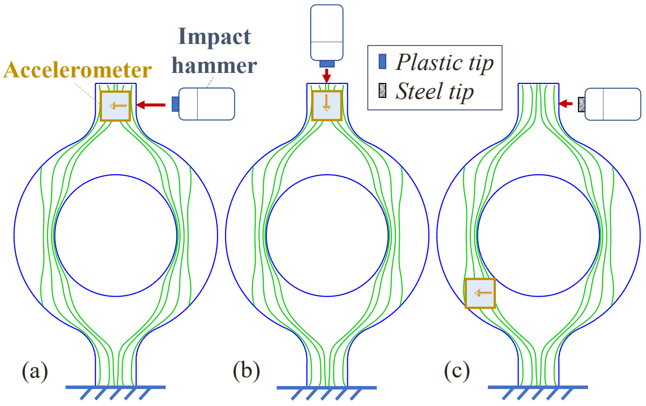

Fig. 12. The impact hammer modal test setup for (a) the first mode, (b) the second mode, (c) the third and fourth high-frequency modes.

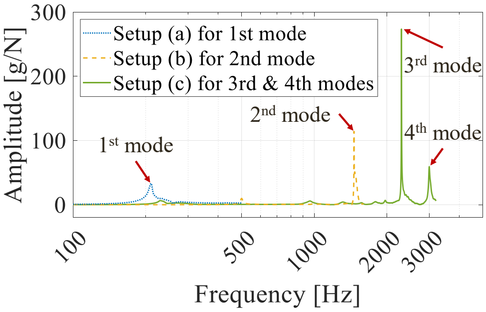

Fig. 13. The frequency response of the loop-shaped specimen in the impact hammer modal tests.

Table 5
Comparing natural frequencies of the loop-shaped specimen from FEM-BFP and the impact hammer modal tests.

	1st mode	2nd mode	3rd mode	4th mode
Resonant frequency [Hz]	210.5	1463	2301	3000
Damping ratio	1.78 %	0.09 %	0.09 %	0.6 %
Natural frequency [Hz] (Experiment)	210.53	1463	2301	3000.05
Natural frequency [Hz] (FEM-BFP simulation)	217.72	1571.82	2453.66	2997.75
Model deviation	3.42 %	7.44 %	6.63 %	0.08 %

Note that the thickness of the part is also increased to 8 mm to reduce the interference vibration in the thickness direction for the impact hammer modal test. According to the mode shape in the simulation, the accelerometer is horizontally installed on the top of the loop-shaped part for the first mode with a horizontal impact shown in Fig. 12(a). Vertical impact and accelerometer installation are adopted for the second mode, as shown in Fig. 12(b). For the third and fourth modes, the accelerometer is horizontally installed on the side of the loop-shaped part, with the impact introduced from the side (Fig. 12(c)). In addition, for these high-frequency modes, a steel tip is used instead of plastic tips to introduce more impact energy at the high frequencies. The magnitudes of the frequency response function are shown in Fig. 13, and the natural frequencies are shown in Table 5. The natural frequencies are calculated from the resonant frequencies given by:

$$\omega_n = \frac{\omega_r}{\sqrt{1-\left(\frac{1}{2Q}\right)^2}}, \quad Q = \frac{\omega_0}{\omega_2-\omega_1}, \tag{75}$$

where ω_n is the natural frequency, ω_r is the resonant frequency, and Q is the damping factor. The 3-dB rule calculates Q by looking at 3-dB-down frequencies ω_1 and ω_2 from the peak frequency ω_0 [39]. According to Table 5, the modal response predictions are verified by the experiment. The errors are observed to be less than 8 %, which arise from the imperfect fiber-matrix interface unavoidable in the manufacturing process, which is omitted in the FEM-BFP formulations. Other resonant peaks with low amplitudes are also observed in the frequency response function. These frequencies are from harmonics and 3D mode shapes that are not considered in the current FEM-BFP model.

Table 6
The parameters for GBFO for the looped specimen.

m	n_c	μ_1 [J^{-1}]	μ_2 [mm^{-1}]	w_p	w_b	p_1	p_2	r_g
5	25	3	0.1	1.96	0.175	9.5	5.9	0.5

4.3. GBFO simulation and experiment verification

4.3.1. Loop-shaped specimen case study

The gradient-based optimization program is implemented with the Poblano optimization toolbox [40]. The load boundary condition is applied on the top and bottom of the part for the tensile simulation. The optimization in this section compares the PSD and the GBFO methods. According to the optimization setup, the detailed GBFO parameters are listed in Table 6. The B-spline's order m and the number of control points n_c are selected to ensure the fiber's degrees of freedom. The parameters μ_1 and μ_2 are selected based on their representative values, with a slight emphasis on μ_1 to highlight the desire to enhance stiffness. The terms w_p, p_1, p_2, and r_g are designed to ensure that the potential function is close to zero at the fiber width and illustrates clear repulsion and attraction regions, as Fig. 5 shows. The term w_b is designed for the minimum distance between the fiber and the boundary. A simple case is performed to ensure the effectiveness of the potential function. The objective function's gradient change is recorded when moving a control point in the x direction shown in Fig. 14. The required minimum distance is 0.35 mm, which equals the width w of a continuous carbon fiber-reinforced thermoset polymer. The gradient increases first when fiber paths move closer to the high-stress region due to the stiffness objective, while its direction reverses to avoid overlapping when the distance is close to the width. The tradeoff study is performed with a minimum fiber distance of 0.4 mm, and the stiffness with increasing numbers of fibers and its contribution to unit length are plotted in Fig. 15. It is observed that the return fiber reinforcement shrinks as the number of fiber paths increases. Based on this study, the number of fiber paths for the part is selected to be eight, formulating an effective tradeoff between stiffness and fiber usage. The GBFO converges after 300 iterations. In each iteration, the objective is evaluated at least four times to update the gradient direction with an average iteration calculation time of 60 s

The optimized fiber paths with the GBFO methods, compared to the PSD method, are plotted in Fig. 16. The corresponding von Mises stress field is also plotted with the FEM-BFP method, providing the stiffness matrices. Note that both the PSD and GBFO methods generate symmetric fiber paths due to the tensile loading conditions. The fiber paths optimized with the GBFO method move close to each other in the middle and neck positions of the specimen. These movements show the tendency of fiber to concentrate at the high-stress region, exploiting the fiber's anisotropic properties to enhance stiffness with reduced fiber usage. Correspondingly, the stiffness of the part generated from the GBFO method illustrates a 27 % enhancement in its tensile direction compared to the PSD method, while reducing 3.9 % of fiber usage.

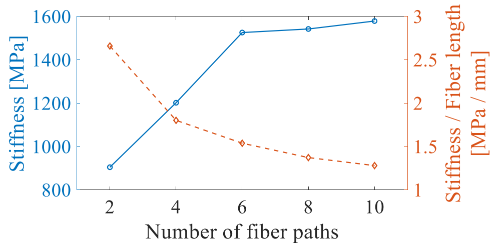

Fig. 15. The stiffness and the stiffness regarding fiber length of the loop-shaped specimen with the PSD method.

The fiber path generated from PSD and GBFO methods are manufactured with the Anisoprint A4 printer discussed in Section 4.1. The specimen has ten layers, including six fiber-reinforced layers and four matrix material layers. To streamline the printing and testing process, pure matrix layers are printed on the top and bottom of the specimen. The classical laminate theory (CLT) [41] is introduced to calculate the actual stiffness of the fiber-reinforced layer to compare the simulation and experiment results. Define the stiffness of the composite layers and the matrix layers are K_c and K_m, respectively, the overall part's stiffness is given by:

$$K_T = K_c h_c + K_m h_m, \tag{76}$$

where h_c and h_m are the total height of the fiber-reinforced and matrix material layer. Accordingly, the stiffness of the pure composite layers is given by:

$$K_c = \frac{K_T - K_m h_m}{h_c}. \tag{77}$$

Multiple loop-shaped specimens are printed with the fiber from PSD and GBFO methods, as shown in Fig. 17. During the tensile tests, the force-displacement relationships are each the average of three specimens from PSD and GBFO methods shown in Fig. 18. The part with the GBFO method achieves higher stiffness and strength than the PSD

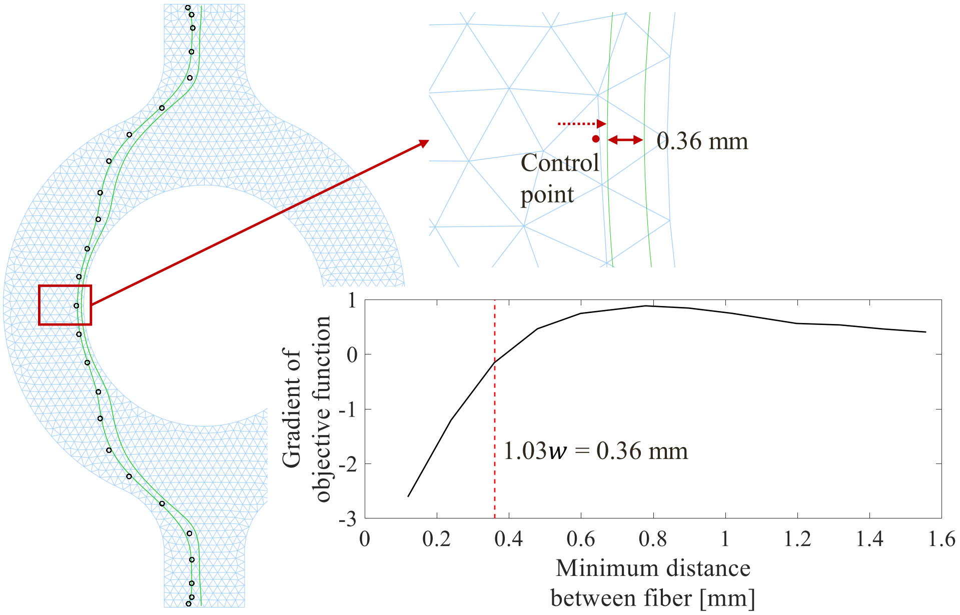

Fig. 14. Change of objective's gradient when the minimum distance between fibers decreases.

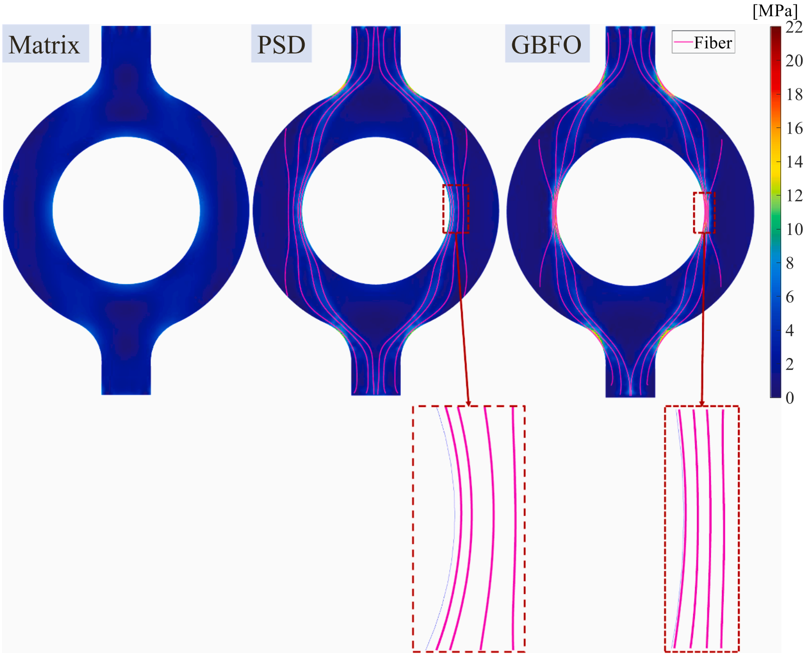

Fig. 16. PSD and GBFO fiber paths and stress fields with FEM-BFP.

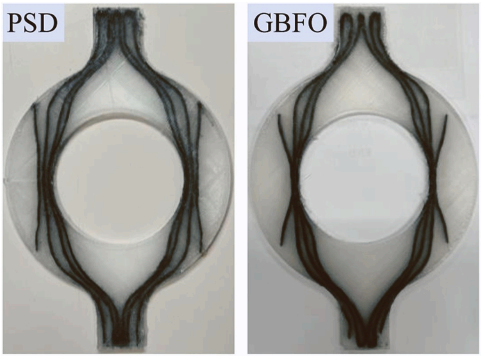

Fig. 17. The loop-shaped specimens with fiber paths generated from the PSD and the GBFO methods.

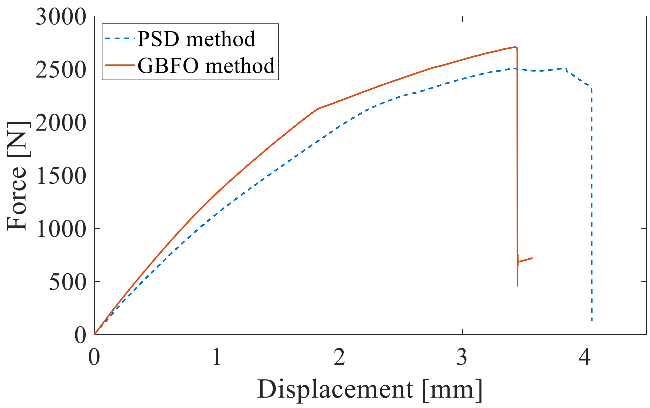

Fig. 18. The force-displacement relationship of the two loop-shaped specimens (with PSD and the GBFO methods) in tensile tests.

Table 7
The optimization result of the loop-shaped specimen with four fiber paths on each side.

	PSD method	GBFO method	Enhancement (reduction)
Stiffness (FEM-BFP) [N/mm]	1493.1	1896.7	27 %
Stiffness (Tensile tests) [N/mm]	1603.1	1880.5	17.3 %
Peak load (Tensile tests) [N]	2504.7	2706.5	8.1 %
Fiber usage [mm]	1137.8	1093.4	− 3.9 %

method. The corresponding stiffness of the composite layers is calculated with Eq. (77) and is summarized in Table 7. Note that the FEM-BFP method provides a relatively accurate estimation of the stiffness of the parts: its prediction errors with the PSD and the GBFO fiber paths are 6.8 % and 0.9 %, respectively. The initial fiber paths were generated by the PSD method, which can be considered a close-to-optimal solution. Hence, the enhancement from the initial fiber paths was not as significant as the optimization result from the unoptimized paths. In the tensile test, the GBFO achieves 17.3 % increases in stiffness and 8.1 % enhancements in strength, highlighting the effectiveness of the proposed method.

4.3.2. Curved cantilever beam case study

An additional curved cantilever beam specimen, inspired by an aircraft seat support beam component, is introduced to highlight the

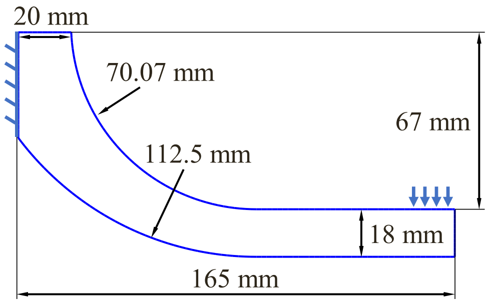

Fig. 19. Curved cantilever beam schematics and loading condition.

Table 8
The parameters for GBFO for the curved cantilever beam.

m	n_c	μ_1 [J^{-1}]	μ_2 [mm^{-1}]	w_p	w_b	p_1	p_2	r_g
5	20	0.1	0.08	1.96	0.175	9.5	5.9	0.5

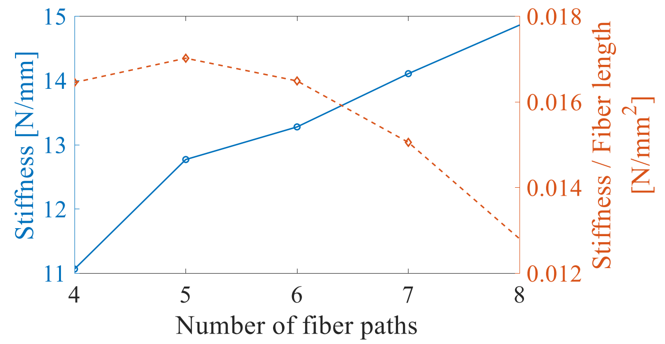

Fig. 20. The stiffness and the stiffness regarding fiber length of the curved cantilever beam with the PSD method.

proposed methods. The beam's schematics and representative loading conditions are shown in Fig. 19. The thickness of the beam is 5 mm. Similar to the loop-shaped specimen, the detailed GBFO parameters of this beam are listed in Table 8. The number of fiber paths is determined to be eight, according to the tradeoff study shown in Fig. 20. The GBFO converges after 181 iterations. The computational speed of each iteration is similar to the loop-shaped specimen.

The PSD and GBFO fiber paths are plotted in Fig. 21. The corresponding von Mises stress field is also plotted with the FEM-BFP method, providing the stiffness matrices. The fiber paths in the beam also tend to concentrate on the high-stress region close to the upper boundary. Correspondingly, the stiffness of the part generated from the GBFO method illustrates a 39.2 % enhancement in its bending direction compared to the PSD method while keeping the same fiber usage. However, the optimized fiber paths have sharp angles, which can weaken the manufacturing quality[42]. A curvature constraint is introduced to the objective function as a soft constraint, which assumes the path's curvature by the angle of any three consecutive control points. The curvature constraint κ is given by:

$$\begin{aligned} \kappa &= \sum_{i=2}^{n_c-1} \sigma_\kappa \left(\arccos \left(\frac{(\mathbf{p}_{c,i-1} - \mathbf{p}_{c,i}) \cdot (\mathbf{p}_{c,i+1} - \mathbf{p}_{c,i})}{\|\mathbf{p}_{c,i-1} - \mathbf{p}_{c,i}\| \|\mathbf{p}_{c,i+1} - \mathbf{p}_{c,i}\|} \right) \right), \\ \sigma_\kappa(r) &= a_\kappa \left(1 - \frac{1}{1 + e^{(-p_\kappa r + \kappa_r)}} \right), \end{aligned} \tag{78}$$

where the angle of three consecutive control points is r. The potential function σ_κ is typically zero but increases significantly when the angle is larger than the constraint. The constraint value is forty degrees defined by the parameters $p_\kappa = 10$ and $\kappa_r = -0.3$; the amplitude $a_\kappa = 50000$ controls the function's increment. The curvature-constrained fiber paths avoid the sharp angle compared with the original GBFO result, as shown in Fig. 22. On the other hand, the curvature-constrained result achieves a 17 % enhancement of the part's stiffness, which is lower than the original result. Note that the optimized fiber paths are connected when printing, leading to sharp angles. This problem of balancing the

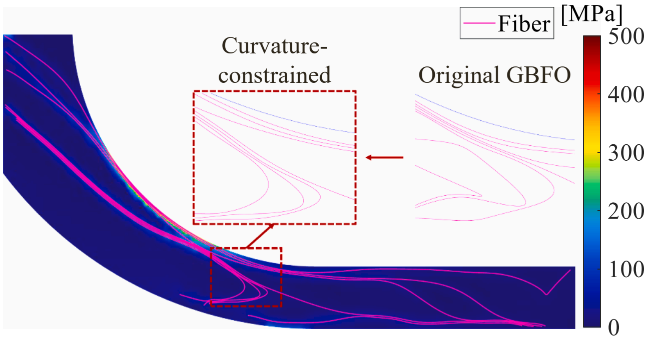

Fig. 22. Curved cantilever beam stress fields with FEM-BFP and fiber paths generated with curvature-constrained GBFO.

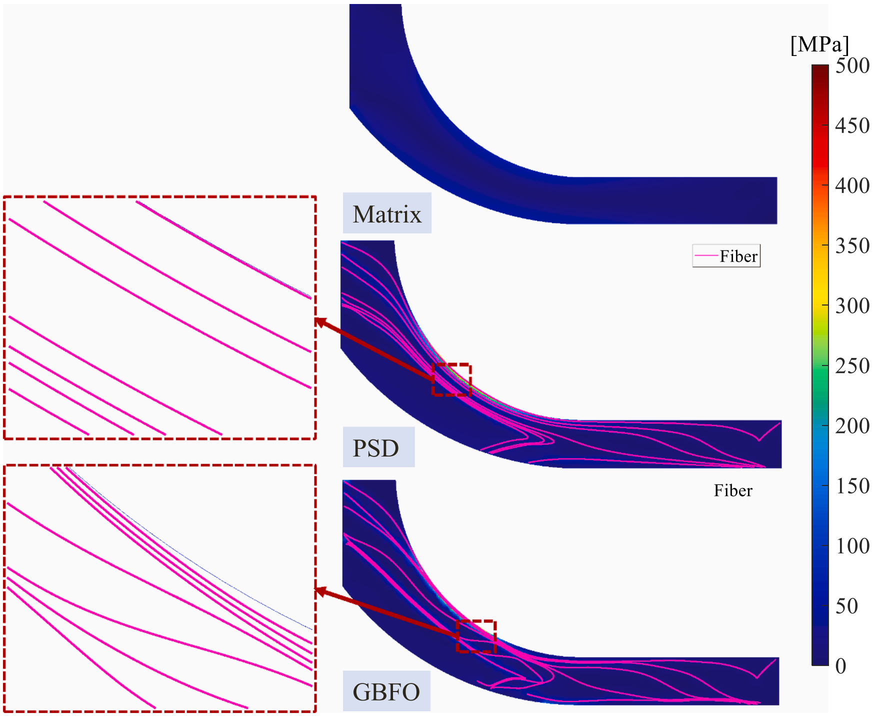

Fig. 21. Curved cantilever beam stress fields with FEM-BFP and fiber paths generated with PSD and GBFO.

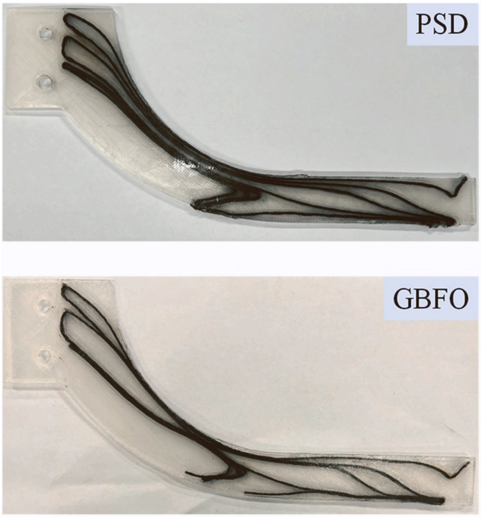

Fig. 23. The beams with fiber paths generated from the PSD and the GBFO methods.

Table 9
The optimization result of the beams with eight fiber paths.

	PSD method	GBFO method	Enhancement (reduction)
Stiffness (FEM-BFP) [N/mm]	22.0061	25.7503	17.01 %
Stiffness (Bending tests) [N/mm]	21.4528	23.97	11.73 %
Peak load (Bending tests) [N]	284.4	243.4	– 14.41 %
Fiber usage [mm]	1160.8	1132.1	– 2.47 %

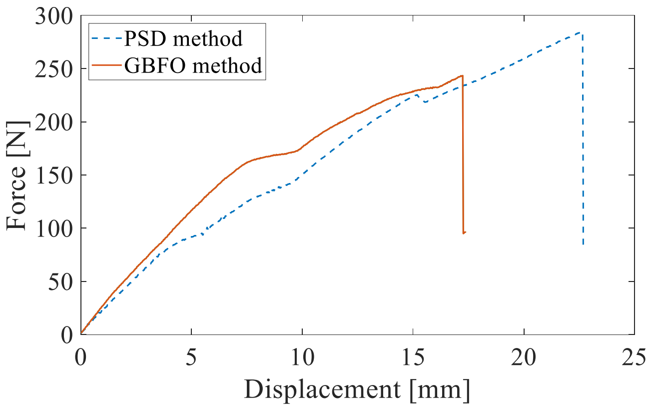

Fig. 24. The force-displacement relationship of the curved cantilever beam (with PSD and the GBFO methods) in bending tests.

mechanical objectives and manufacturing quality could be addressed by separating the optimized paths and reconnecting at the turning points.

Following the simulation, the PSD and GBFO methods each printed three specimens for the bending test, as shown in Fig. 23. The test result is summarized in Table 9, and the force-displacement relationships are shown in Fig. 24. In the bending test, an 11.73 % enhancement is observed. Note that the beam's stiffness from the GBFO method is 6.9 % lower than the prediction. This error is mainly caused by the overestimation of the compressive performance of the fiber. The GBFO method assumes the stiffness of fiber under compression is equivalent to its tensile stiffness. The initial fiber paths generated by the PSD method try to avoid the compression stress field by tracing the positive stress, but the GBFO method tends to cover the high-stress region without distinguishing. This type of error could be addressed by introducing the separation strategy to analyze the compressive region with different material properties. Due to the large deformation in the test, the predicted stiffness represents the stiffness at the initial elastic deformation stage. The following mechanical behavior can be predicted by iteratively updating the FEM equations during the part's deformation. Moreover, the curved cantilever beam case observes higher peak force and larger fracture displacement of specimens from the PSD method than the GBFO method. This arises because more shear force is applied at the matrix and fiber bonding interface. Therefore, the early failure of the GBFO method arises from its relatively close fiber layouts. The optimization problem optimizes compliance, and the ultimate strength is not the objective addressed in this work. The minimum compliance objective (i.e., stiffness optimization) is a standard objective for topology optimization in most engineering cases and thus is adopted in the GBFO method based on the standard FEM framework. The established FEM in this work describes other mechanical behaviors, such as natural frequency, weight, and flexibility of the part, which can be alternative objectives.

5. Conclusion

This paper addressed the continuous fiber path optimization problem in additive manufacturing by establishing a semi-analytical finite element model with B-spline fiber parameterization (FEM-BFP) and gradient-based fiber path optimization (GBFO). The FEM-BFP defined an analytical fiber-in-element probability, thus bypassing the computationally intensive determination of fiber-element intersection. The probability, along with the convex hulls of the B-spline, enabled a convenient evaluation of the local stiffness and mass matrix increments. These increments were assembled to acquire the global stiffness and mass matrices, leading to the effective and efficient prediction of loading responses, stiffness, natural frequencies, etc. The accuracy and effectiveness of the FEM-BFP method were verified compared with commercial software Abaqus, tensile tests, and impact hammer modal tests. With the FEM-BFP and its probabilistic framework, the gradients of the stiffness and mass matrix regarding the fiber B-spline control points were conveniently established, leading to GBFO with objective functions minimizing compliance and fiber usage. Additional constraints on the fiber-to-fiber and fiber-to-boundary distances were also introduced to the optimization via a continuous potential function with explicit gradients. The results of GBFO were compared with a principal stress direction method, generating the fiber paths that align with the maximum stress direction. In the simulation and experiments, the parts with fiber generated with the GBFO method illustrated an enhancement in stiffness with less fiber usage.

CRediT authorship contribution statement

Shuaiyin He: Writing – original draft, Visualization, Validation, Software, Methodology, Investigation. **Peng-Cheng Ma:** Writing – review & editing, Visualization. **Molong Duan:** Writing – review & editing, Writing – original draft, Visualization, Validation, Supervision, Software, Resources, Project administration, Methodology, Investigation, Funding acquisition, Formal analysis, Data curation, Conceptualization.

Declaration of Generative AI and AI-assisted technologies in the writing process

During the preparation of this work, the authors used ChatGPT and Grammarly AI to perform grammar checks. After using these tools, the authors reviewed and edited the content as needed and took full responsibility for the content of the publication.

Declaration of Competing Interest

The authors declare that they have no known competing financial interests or personal relationships that could have appeared to influence the work reported in this paper.

Data availability

Data will be made available on request.

Acknowledgement

The authors acknowledge support from the HKUST Research Equipment Development Fund and HKUST Bridge Gap Fund (BGF). This work was partly supported by the Project of Hetao Shenzhen-Hong Kong Science and Technology Innovation Cooperation Zone (HZQB-KCZYB-2020083). Profs. Wenjing Ye, Kai Tang, and Yangyang Chen provided valuable feedback to this work. The help from the funding agency and the other researchers is sincerely appreciated.

References

[1] S. Prashanth, K. Subbaya, K. Nithin, S. Sachhidananda, Fiber reinforced composites - a review, J. Mater. Sci. Eng. 06 (2017), https://doi.org/10.4172/2169-0022.1000341.

[2] A.V. Azarov, F.K. Antonov, M.V. Golubev, A.R. Khaziev, S.A. Ushanov, Composite 3D printing for the small size unmanned aerial vehicle structure, Compos. Part B Eng. 169 (2019) 157–163, https://doi.org/10.1016/j.compositesb.2019.03.073.

[3] S. Erden, K. Ho, Fiber Technology for Fiber-Reinforced Composites, Elsevier, 2017, https://doi.org/10.1016/C2015-0-05497-1.

[4] M.D. Wakeman, T.A. Cain, C.D. Rudd, R. Brooks, A.C. Long, Compression moulding of glass and polypropylene composites for optimised macro- and micro-mechanical properties II. Glass-mat-reinforced thermoplastics, Compos. Sci. Technol. 59 (1999) 709–726, https://doi.org/10.1016/S0266-3538(98)00124-9.

[5] L.G. Blok, M.L. Longana, H. Yu, B.K.S. Woods, An investigation into 3D printing of fibre reinforced thermoplastic composites, Addit. Manuf. 22 (2018) 176–186, https://doi.org/10.1016/j.addma.2018.04.039.

[6] L.C. Hollaway, Advanced fibre-reinforced polymer (FRP) composite materials for sustainable energy technologies, in: in: Adv. Fibre-Reinforced Polym. Compos. Struct. Appl., Elsevier, 2013, pp. 737–779, https://doi.org/10.1533/9780857098641.4.737.

[7] B. Koon, N. Stranberg, Development and application of continuous fiber 3D printing process for aerospace, Int. SAMPE Tech. Conf. (2021) 1223–1234, https://doi.org/10.33599/nasampe/s.21.0598.

[8] D. Tobalina-Baldeon, F. Sanz-Adan, M.A. Martinez-Calvo, J. Santamaría-Pena, Dynamic tensile stress-compressive stress behavior of thermoplastic matrix composite materials reinforced with continuous fiber for automotive damping and anti-vibration structural elements, Materials 13 (2019) 5, https://doi.org/10.3390/ma13010005.

[9] B. Sobhani Aragh, E. Borzabadi Farahani, B.X. Xu, H. Ghasemnejad, W.J. Mansur, Manufacturable insight into modelling and design considerations in fibre-steered composite laminates: state of the art and perspective, Comput. Methods Appl. Mech. Eng. 379 (2021) 113752, https://doi.org/10.1016/j.cma.2021.113752.

[10] D. Rajpal, F.M.A. Mitrotta, C.A. Socci, J. Sodja, C. Kassapoglou, R. De Breuker, Design and testing of aeroelastically tailored composite wing under fatigue and gust loading including effect of fatigue on aeroelastic performance, Compos. Struct. 275 (2021) 114373, https://doi.org/10.1016/j.compstruct.2021.114373.

[11] P.K. Penumakala, J. Santo, A. Thomas, A critical review on the fused deposition modeling of thermoplastic polymer composites, Compos. Part B Eng. 201 (2020) 108336, https://doi.org/10.1016/j.compositesb.2020.108336.

[12] P. Zhuo, S. Li, I.A. Ashcroft, A.I. Jones, Material extrusion additive manufacturing of continuous fibre reinforced polymer matrix composites: A review and outlook, Compos. Part B Eng. 224 (2021) 109143, https://doi.org/10.1016/j.compositesb.2021.109143.

[13] N. Van De Werken, H. Tekinalp, P. Khanbolouki, S. Ozcan, Additively manufactured carbon fiber-reinforced composites: state of the art and perspective, Addit. Manuf. 31 (2020) 100962, https://doi.org/10.1016/j.addma.2019.100962.

[14] D. Bi, M. Duan, T.Y. Lau, F. Xie, K. Tang, Strength-enhanced volume decomposition for multi-directional additive manufacturing, Addit. Manuf. 69 (2023) 103529, https://doi.org/10.1016/j.addma.2023.103529.

[15] S. Chen, Y. Yang, S. Liu, M. Duan, In-situ additive manufacturing deposition trajectory monitoring and compensation with thermal camera, Addit. Manuf. 78 (2023) 103820, https://doi.org/10.1016/j.addma.2023.103820.

[16] S.M.F. Kabir, K. Mathur, A.M. Seyam, A critical review on 3D printed continuous fiber-reinforced composites: history, mechanism, materials and properties, Compos. Struct. 232 (2020) 111476, https://doi.org/10.1016/j.compstruct.2019.111476.

[17] A. Uşun, R. Gümrük, The mechanical performance of the 3D printed composites produced with continuous carbon fiber reinforced filaments obtained via melt impregnation, Addit. Manuf. 46 (2021) 102112, https://doi.org/10.1016/j.addma.2021.102112.

[18] D. Jiang, D.E. Smith, Anisotropic mechanical properties of oriented carbon fiber filled polymer composites produced with fused filament fabrication, Addit. Manuf. 18 (2017) 84–94, https://doi.org/10.1016/j.addma.2017.08.006.

[19] B. Brenken, E. Barocio, A. Favaloro, V. Kunc, R.B. Pipes, Fused filament fabrication of fiber-reinforced polymers: a review, Addit. Manuf. 21 (2018) 1–16, https://doi.org/10.1016/j.addma.2018.01.002.

[20] M. Heidari-Rarani, M. Rafiee-Afarani, A.M. Zahedi, Mechanical characterization of FDM 3D printing of continuous carbon fiber reinforced PLA composites, Compos. Part B Eng. 175 (2019) 107147, https://doi.org/10.1016/j.compositesb.2019.107147.

[21] S. Yuan, S. Li, J. Zhu, Y. Tang, Additive manufacturing of polymeric composites from material processing to structural design, Compos. Part B Eng. 219 (2021) 108903, https://doi.org/10.1016/j.compositesb.2021.108903.

[22] J. Naranjo-Lozada, H. Ahuett-Garza, P. Orta-Castañón, W.M.H. Verbeeten, D. Sáiz-González, Tensile properties and failure behavior of chopped and continuous carbon fiber composites produced by additive manufacturing, Addit. Manuf. 26 (2019) 227–241, https://doi.org/10.1016/j.addma.2018.12.020.

[23] R.R. Fernandes, N. van de Werken, P. Koirala, T. Yap, A.Y. Tamijani, M. Tehrani, Experimental investigation of additively manufactured continuous fiber reinforced composite parts with optimized topology and fiber paths, Addit. Manuf. 44 (2021) 102056, https://doi.org/10.1016/j.addma.2021.102056.

[24] H. Zhang, D. Yang, Y. Sheng, Performance-driven 3D printing of continuous curved carbon fibre reinforced polymer composites: a preliminary numerical study, Compos. Part B Eng. 151 (2018) 256–264, https://doi.org/10.1016/j.compositesb.2018.06.017.

[25] T. Wang, N. Li, G. Link, J. Jelonnek, J. Fleischer, J. Dittus, D. Kupzik, Load-dependent path planning method for 3D printing of continuous fiber reinforced plastics, Compos. Part A Appl. Sci. Manuf. 140 (2021) 106181, https://doi.org/10.1016/j.compositesa.2020.106181.

[26] T. Liu, S. Yuan, Y. Wang, Y. Xiong, J. Zhu, L. Lu, Y. Tang, Stress-driven infill mapping for 3D-printed continuous fiber composite with tunable infill density and morphology, Addit. Manuf. 62 (2023) 103374, https://doi.org/10.1016/j.addma.2022.103374.

[27] X. Chen, G. Fang, W.-H. Liao, C.C.L. Wang, Field-based toolpath generation for 3d printing continuous fibre reinforced thermoplastic composites, Addit. Manuf. 49 (2022) 102470, https://doi.org/10.1016/j.addma.2021.102470.

[28] T. Heitkamp, S. Kuschmitz, S. Girnth, J.-D. Marx, G. Klawitter, N. Waldt, T. Vietor, Stress-adapted fiber orientation along the principal stress directions for continuous fiber-reinforced material extrusion, Prog. Addit. Manuf. 8 (2022) 541–559, https://doi.org/10.1007/s40964-022-00347-x.

[29] T. Suzuki, S. Fukushige, M. Tsunori, Load path visualization and fiber trajectory optimization for additive manufacturing of composites, Addit. Manuf. 31 (2020) 100942, https://doi.org/10.1016/j.addma.2019.100942.

[30] K. Sugiyama, R. Matsuzaki, A.V. Malakhov, A.N. Polilov, M. Ueda, A. Todoroki, Y. Hirano, 3D printing of optimized composites with variable fiber volume fraction and stiffness using continuous fiber, Compos. Sci. Technol. 186 (2020) 107905, https://doi.org/10.1016/j.compscitech.2019.107905.

[31] Z. Hou, X. Tian, J. Zhang, Z. Zheng, L. Zhe, D. Li, A.V. Malakhov, A.N. Polilov, Optimization design and 3D printing of curvilinear fiber reinforced variable stiffness composites, Compos. Sci. Technol. 201 (2021) 108502, https://doi.org/10.1016/j.compscitech.2020.108502.

[32] V.S. Papapetrou, C. Patel, A.Y. Tamijani, Stiffness-based optimization framework for the topology and fiber paths of continuous fiber composites, Compos. Part B. 183 (2020) 107681, https://doi.org/10.1016/j.compositesb.2019.107681.

[33] G.W. Melenka, B.K.O. Cheung, J.S. Schofield, M.R. Dawson, J.P. Carey, Evaluation and prediction of the tensile properties of continuous fiber-reinforced 3D printed structures, Compos. Struct. 153 (2016) 866–875, https://doi.org/10.1016/j.compstruct.2016.07.018.

[34] D.L. Logan, A First Course in the Finite Element Method, Nelson, 2007.

[35] M. Duan, S. He, Continuous fiber path optimization in composite additive manufacturing, in: Proc. of the ASME 2023 Manuf. Sci. Eng. Conf., New Brunswick, US, 2023.

[36] Anisoprint, Basic sPecifications, (n.d.). ⟨https://anisoprint.com/solutions/desktop/⟩.

[37] ASTM, Standard Test Method for Tensile Properties of Plastics (2022) 16, https://doi.org/10.1520/D0638-22.

[38] J. Koko, A Matlab mesh generator for the two-dimensional finite element method, Appl. Math. Comput. 250 (2015) 650–664, https://doi.org/10.1016/j.amc.2014.11.009.

[39] R. Huňady, F. Trebuňa, M. Hagara, M. Schrötter, The use of Modan 3D in experimental modal analysis, Appl. Mech. Mater. 486 (2013) 36–41, https://doi.org/10.4028/www.scientific.net/AMM.486.36.

[40] D.M. Dunlavy, T.G. Kolda, E. Acar, Poblano v1.0: a Matlab Toolbox for Gradient-Based Optimization (2010).

[41] P. Kumar Mishra, S. P, Prediction of in-plane stiffness of multi-material 3D printed laminate parts fabricated by FDM process using CLT and its mechanical behaviour under tensile load, Mater. Today Commun. 23 (2020) 100955, https://doi.org/10.1016/j.mtcomm.2020.100955.

[42] Y. Huang, G. Fang, T. Zhang, C.C.L. Wang, Turning-angle optimized printing path of continuous carbon fiber for cellular structures, Addit. Manuf. 68 (2023) 103501, https://doi.org/10.1016/j.addma.2023.103501.